Performance Analysis for Synthetic Aperture Radar Target Classification

by

Choongyeun Cho

B.S., Electronics Engineering
Korea University, 1998

Submitted to the Department of Electrical Engineering and Computer Science
in partial fulfillment of the requirements for the degree of

Master of Science in Electrical Engineering

at the

MASSACHUSETTS INSTITUTE OF TECHNOLOGY

February 2001

Author .....
Department of Electrical Engineering and Computer Science
September 29, 2000

Certified by .....
Professor Jeffrey H. Shapiro
Julius A. Stratton Professor of Electrical Engineering
Thesis Supervisor

Accepted by .....
Arthur C. Smith
Chairman, Department Committee on Graduate Students

Performance Analysis for Synthetic Aperture Radar Target Classification

by

Choongyeun Cho

Submitted to the Department of Electrical Engineering and Computer Science
on September 29, 2000, in partial fulfillment of the
requirements for the degree of
Master of Science in Electrical Engineering

Abstract

In recent years, synthetic aperture radars (SARs) have been used to detect man-made targets and to distinguish them from naturally occurring background. The purpose of this thesis is to assess target classification performance of a SAR-based automatic target recognition (ATR) system – starting from a foundation of rigorous, physics-based signal models developed from electromagnetic scattering theory – without incurring the restrictive assumptions made in previous work.

Targets consist of a repertoire of geometrically-simple reflectors, and the performance discrepancy of a conventional full-resolution processor with respect to a multi/adaptive-resolution processor is discussed. The analytical computation of target classification performance is generally demanding due to the dense correlation between the likelihood values of different targets. Thus most of our attention is devoted to obtaining upper and lower bounds on probability of correct classification (PCC). Three types of target conditions are investigated: (1) targets consisting of a known constellation of reflector components at known absolute locations; (2) targets consisting of a constellation of known reflector components which are located at random positions within some limited, prescribed uncertainty regions; and (3) targets consisting of a constellation of known reflector components with known centroid location but unknown rotation about that centroid. For settings 1 and 2, we obtain a lower bound on PCC from the performance of a recognition processor that makes component-wise reflector decisions, and we obtain an upper bound on PCC by assuming that the returns from a target's reflector components have known relative phases. Computer simulations show that the lower bound is very close to the exact result. For setting 3, we use the Laplace approximation to obtain an approximation to PCC that is valid at high signal-to-noise ratios.

Thesis Supervisor: Professor Jeffrey H. Shapiro
Title: Julius A. Stratton Professor of Electrical Engineering

Acknowledgments

First, I would like to express my sincere gratitude to my research advisor, Professor Jeffrey H. Shapiro for his support and guidance. He has been always willing to give me insights and pointers to tackle the problems along the way. Also, I am grateful to Chen-Pang Yeang for his continuous interest in my research and detailed help through a number of informal meetings. Lastly I thank my parents, Gilja Kwon and Namjo Cho, for their love and belief in me. Without their love and prayer I couldn't have been here getting the finest education in the first place. I acknowledge the gracious financial support from U.S. Air Force Office of Scientific Research Grant F49620-96-1-0028.

Contents

List of Figures

List of Tables

Chapter 1

Introduction

1.1 Background

In recent years, synthetic aperture radars (SARs) have been rapidly gaining prominence in applications such as remote sensing, surface surveillance, and automatic target recognition (ATR). SAR is a microwave radar imaging system usually mounted on an airborne or spaceborne craft, capable of imaging terrain and targets at a fine resolution by artificially synthesizing a large aperture antenna. Advantages of using microwave radar over optical imaging techniques include the ability to penetrate cloud cover, and to image terrain at night. Microwave imaging systems are at a disadvantage, however, in that they require an impractically long antenna to produce the narrow beamwidth required to achieve the same imaging resolution as optical systems. SAR systems overcome this limitation by emulating a sufficiently long "synthetic" antenna aperture by obtaining multiple measurements of the terrain's reflectivity as the SAR platform moves across the terrain. The multiple returns are then coherently processed as measurements from an array of sensors phased as a beamformer antenna, thus providing a high imaging resolution. A SAR can be interpreted either as a radar system with a phased-array antenna, or as a radar system in which the radar return contains a frequency chirp along the cross-range direction due to its time-dependent propagation delay [1]. From both perspectives, the enhanced spatial resolution is obtained via appropriate signal processing.

A SAR-based ATR system requires a fast and effective discriminator to suppress natural clutter, to detect the presence of a target, and to classify the type of target from its radar return [2]. Such a system relies on models for the different components of the radar return, namely, the returns from different types of man-made targets, natural clutter, and background noise.

One typical approach is to model the target return as a parametrized deterministic signal pattern, and the clutter and noise as stochastic processes characterized by their statistics. In [3], the clutter and noise are modeled as Gaussian random processes with given covariance matrices, and the target return is modeled as a pre-specified spatio-temporal pattern multiplied by complex-amplitude parameters. In [4], the target return is composed of the contributions from several scattering centers. Each scattering-center component contains an amplitude and phase which are determined by the radar's carrier frequency and look angle plus the scattering centers' positions. The unwanted part of the radar return, i.e. the noise, is assumed to be a white-Gaussian process. In [5], the target signal is taken to be a Gaussian intensity function, the clutter a sinusoid with random phase, and the noise a Gaussian process.

Another approach to radar-signal modeling assumes that the target return and the unwanted part (clutter plus noise) are random processes characterized by different statistics. In [6], the target return consisted of a deterministic part and a random part, with the latter coming from scattering-amplitude and scattering-center uncertainties. In [7], the radar signal is a target return multiplied by an uncorrelated speckle noise; the covariance matrices of the target return and the speckle noise are estimated by principal-component analysis. This approach also implies that different clutter types have different statistics. The work in [8] models the full polarimetric radar clutter as a product of a gamma-distributed textural variable and a Gaussian random vector whose covariance matrix is determined empirically. The numerical values for the covariance-matrix elements calculated from real SAR data are different for trees, shadows, grass, and mixed scrub.

Recent studies on multiresolution radar images have revealed a promising potential to enhance target classification performance. In [9] it is shown that, based on the

different variation-vs.-resolution patterns of targets and clutter, discrimination can be accomplished via adaptive multiresolution processing.

None of the above works is founded on a rigorous, physics-based theory which relates the radar return from targets and clutter to their respective physical characteristics in terms of an electromagnetic scattering model. This thesis work is based on the physics-based modeling of SAR imagery, taking into account the effects of the transmitter pulse shape, antenna beam pattern, and free-space wave propagation, previously developed in [10]. Radar return signals from target and from clutter sources are modeled via electromagnetic scattering theory, and as for the signal processor models, a conventional processor, an adaptive-resolution processor, and an optimum whitening-filter processor are presented.

The operational conditions cover two-dimensional imaging, using chirp-pulse waveforms, and full polarimetric data collection. To reflect real SAR operation, targets of interest are assumed to have a repertoire of geometrically simple smaller reflectors. For these physics-based signal and processor models, it is worthwhile to analyze the performance of a SAR-based target classifier. Prior work [10] has given a preliminary assessment of classification performance but was limited to target configurations in which target component locations are known and known to satisfy an orthogonality condition. Thus, this thesis work concentrates on the problem of performance assessment of SAR-based ATR system under less restrictive conditions, comparing the performance of full physics-based signatures to more conventional imaging based on the signal models previously developed by Yeang [10].

1.2 Thesis Outline

This thesis is organized as follows. In chapter 2, the basic principles and geometry of a SAR system are briefly introduced. Then, we present the radar signal models and SAR processor models. With these models, we show how optimum multi-component target classification is done, based on a maximum aposteriori probability rule.

In chapter 3, we focus on a target setting in which each target component can

be located anywhere consistent with the orthogonality condition. It is impractical or even impossible to obtain a direct analytic form of probability of correct classification (PCC) for this case, mainly because the statistics of likelihood values of different targets needed to calculate the PCC are, in general, densely correlated. Therefore, we get around this problem of obtaining PCC by deriving lower and upper bounds on PCC. A valid PCC lower bound can be obtained by finding PCC for any sub-optimal target classifier. We use a "component-wise target recognizer" for a sub-optimal target classifier. It is learned that this sub-optimal classifier performs almost as well as the optimal one. The PCC upper bound is obtained by finding PCC for the case in which we have complete knowledge about the relative phase of each target component, which was assumed to be uniformly random otherwise. Since we have more information for target classification, the classification performance will be improved, thus offering a valid PCC upper bound. Given the complete phase information, the classification task collapses to the problem of M-ary detection of signals in an additive Gaussian noise channel. Still there is no closed-form formula for the probability of error for this problem; thus, we use another weaker inequality to upper bound PCC.

In chapter 4, we deal with a case in which the target components can be located at uniformly-distributed random positions within a given uncertainty area. The classification process entails the usage of a "maximization operation" over the component-location uncertainty region; for the non-random position case, we would have sampled at the known component positions. Due to this maximization, the statistical structure of the likelihood ratios, is complicated and difficult to formulate in an analytic form. We introduce 1-D and 2-D level crossing theory to cope with this problem of expressing the probability densities of the likelihood-ratio-related values, that are needed to calculate PCC. Once the probabilistic structure of these likelihood ratios is specified, the approaches to obtain upper and lower bound on PCC parallel those in chapter 3.

In chapter 5, we investigate the target setting in which the target components form a fixed constellation that is randomly rotated around its center. The likelihood ratios

for this target-component condition depend on the pose angle, and integration over pose angle can be evaluated only by numerical methods. We use the Laplace method to obtain an approximation to PCC that is valid at high signal-to-noise (SNR) ratio.

In chapter 6, a brief summary of this thesis and the further research possibilities are discussed.

Chapter 2

System Models

2.1 Principles of SAR

The scenario for a two-dimensional stripmap-mode and spotlight-mode SAR is sketched in Figure 2-1. The radar antenna and receiver are mounted on an aircraft flying with velocity $\bar{v} = \hat{x}v$ at an altitude L m. Thus the position of the aircraft can be described by the vector $\bar{r}_t = \hat{x}vt + \hat{z}L$.

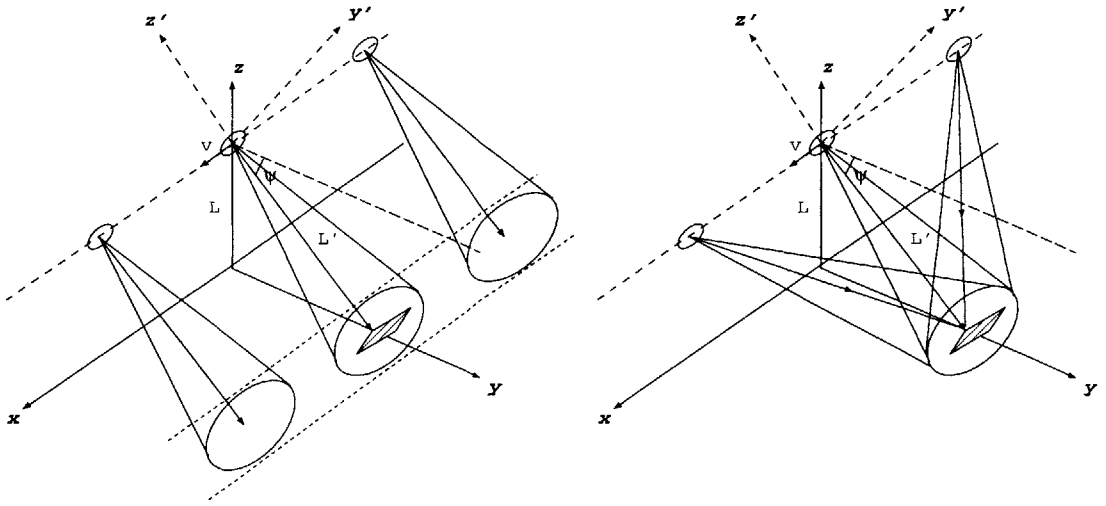

Figure 2-1: Flight geometry for a 2-D stripmap-mode (left) and spotlight-mode SAR (right)

The purpose of SAR is to improve the radar's spatial resolution. The fundamen-

tal principle of a 1-D CW synthetic aperture operation can be explained as follows [11]. For a continuous-wave down-looking radar imager, the Doppler-shift time history associated with the return from a point scatterer is a frequency chirp of rate $\dot{\nu}_D = -2v^2/\lambda_c L$. The time duration of the chirp, T, is the length of time during which the scatterer lies within the radar antenna beam; we shall presume far-field diffraction-limited operation, so that $T \approx \lambda_c L/vd$. Compressing this chirped radar return through a matched filter then yields a time-domain output waveform of duration x_{res}/v, where

$$x_{res} \approx \frac{v}{|\dot{\nu}_D|T} \approx \frac{d}{2} << \frac{\lambda_c L}{d}, \tag{2.1}$$

thus providing along-track (cross-range) spatial resolution that is much better than the diffraction-limited beamwidth of the real antenna aperture. For extended targets, the chirp duration is determined by the target's scattering pattern; a large specular reflector will have a chirp duration much smaller than the dwell time, a fact which an optimum receiver for that target will exploit.

For stripmap-mode operation, the normal direction of the antenna aperture, $-\hat{z}' = -\hat{z}\sin(\psi) + \hat{y}\cos(\psi)$, is on the plane perpendicular to the velocity vector $\hat{x}$ and tilted downward from the horizontal direction $\hat{y}$ with angle ψ, making $L' = L/\sin(\psi)$ the range to the ground. As the aircraft flies, the footprint of the antenna beam swept along the ground is an elongated strip at distance $L/\tan\psi$ from the projection of aircraft trajectory with width $\lambda_c L/d\sin(\psi)$, where d is radar's effective antenna diameter and λ_c is its wavelength. The only difference between the stripmap- and spotlight-mode operations is the normal direction of antenna aperture.

For spotlight-mode operation, the normal direction of antenna aperture is adjusted along the flight path to constantly point toward the region centered at $(x, y, z) = (0, L\cot(\psi), 0)$. The principal advantage of spotlight-mode SAR over conventional stripmap-mode SAR is its enhanced resolution thanks to the fact that the duration that a region of interest is illuminated can be arbitrarily long in principle.

2.2 Radar Signal Model

In [10], Yeang used a first-principles approach to set up signal models of SAR imagery via electromagnetic scattering theory. Since we are interested in quantifying, from a fundamental-principles viewpoint, the target-classification performance advantage of multiresolution/adaptive-resolution processors as compared to conventional SAR imagers, the multi-component target models do not have to be as complicated as a real-world object, such as a tank or truck. They could be simple, but embody the characteristics that highlight the performance differences between conventional SAR full-resolution processing and multiresolution/adaptive-resolution processing.

In this thesis the targets consist of a repertoire of geometrically-simple reflectors, such as a specular mirror (a square flat plate with a perfectly conducting surface), and a dihedral reflector (two perfectly-conducting rectangular plates whose edges meet at a right angle). The PCC bounds that we develop can, for the most part, be easily extended to treat other reflectors, such as trihedrals and dielectric volumes.

In addition to the target return, clutter needs to be modeled. Clutter typically refers to the radar return from anything other than the desired target. It is assumed to be reflection from an infinite-extent rough ground surface.

The final element in the radar signal model is receiver noise. Typically, this is thermal noise, and has a white spectrum. The receiver noise is assumed to be a zero-mean, circulo-complex, vector-Gaussian stochastic process that is white in all its domains.

2.3 SAR Processor Models

2.3.1 Adaptive-resolution Processor

In this thesis work, two types of SAR image processing systems are considered: an adaptive-resolution processor and a whitening-filter processor. An adaptive-resolution processor is a conventional SAR processor with adjustable processing durations. Figure 2-2 illustrates an adaptive-resolution processor for stripmap-mode operation; the

incoming radar return is passed through chirp compression filters in both the cross-range and range domains, and then is video detected to form a radar intensity image. A conventional 2-D stripmap SAR processor uses chirp-compression filters that are matched filters for the radar return from a point scatterer. An extended target can have a very different return duration than that from a point scatterer. Thus our adaptive-resolution processor will optimize the processing durations to achieve best detection performance for such an extended target.

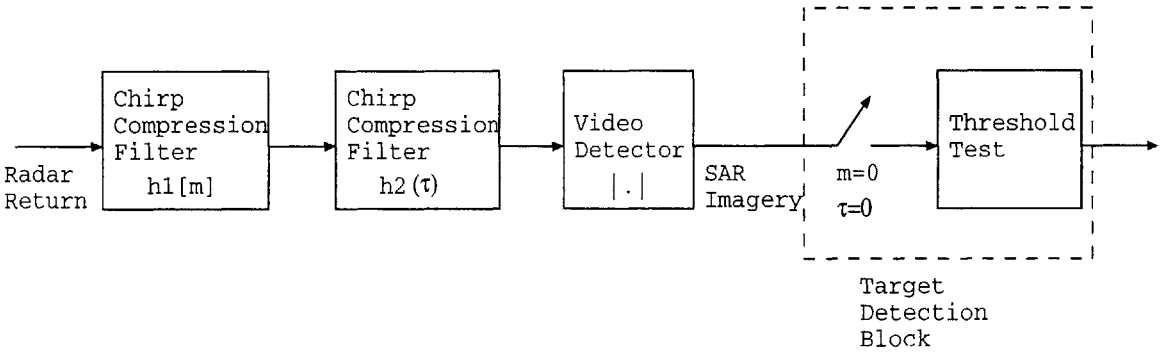

Figure 2-2: Block diagram of adaptive-resolution stripmap-mode SAR processor for detecting a single reflector at a known location

In spotlight-mode operation, a standard interpretation of the radar return is to conceive it as a convolved form of the 2-D Fourier transform of the terrain reflectivity profile, namely, the tomographic rendition of the terrain-reflectivity distribution [12]. An adaptive-resolution spotlight-mode SAR processor first dechirps the radar-return signal along the range and cross-range directions, then samples the de-chirped signal. The sampled signal, after rearrangement by a polar formatter, then undergoes a 2-D discrete Fourier transform operation as shown in Figure 2-3. In this processor, the cross-range processing duration and the range processing duration are variables which determine the resolution.

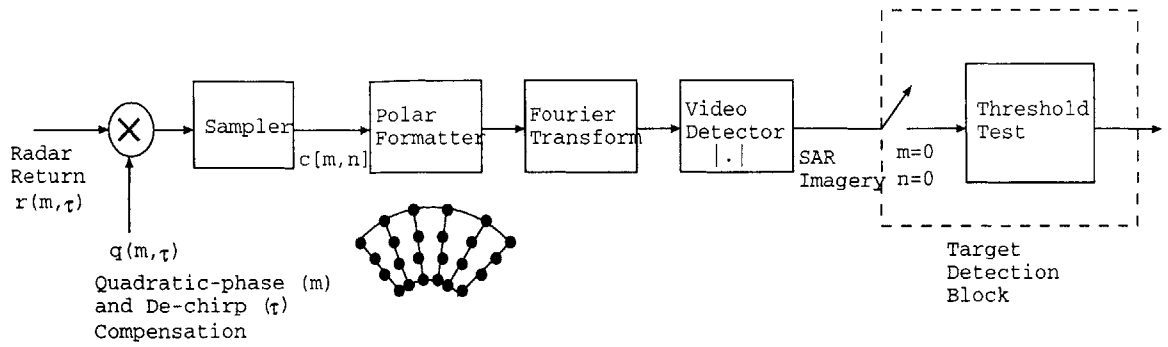

Figure 2-3: Block diagram of adaptive-resolution spotlight-mode SAR processor for detecting a single reflector at a known location

2.3.2 Whitening Processor

Whereas the adaptive-resolution schemes just described can enhance SAR image resolution, they do not, in general, represent optimum receivers. The optimum Neyman-Pearson processing scheme uses a filter to whiten the clutter plus noise, followed by a matched filter corresponding to the target-return waveform passed through the whitening filter, followed in turn by video detection, sampling, and a threshold test. Essentially, the whitening processors for stripmap- and spotlight-model are the same except that for the spotlight-mode we need a time-shifter at its front end in order to compensate the parabolic time-shift of the IF complex envelope of radar return. Figure 2-4 illustrates the whitening-filter optimum processor for spotlight-mode operation.

The whitening-filter processor is seldom as practical as the adaptive-resolution processor because it requires exact knowledge of the clutter and noise statistics and the waveforms scattered from the target types of interest. Nevertheless, the whitening-filter processor is conceptually important in that it is the optimum processor for target classification. As such, its performance in terms of probability of correct classification bounds the performance of any realizable processor. By comparing the classification performance of an adaptive-resolution processor with that of a whitening processor,

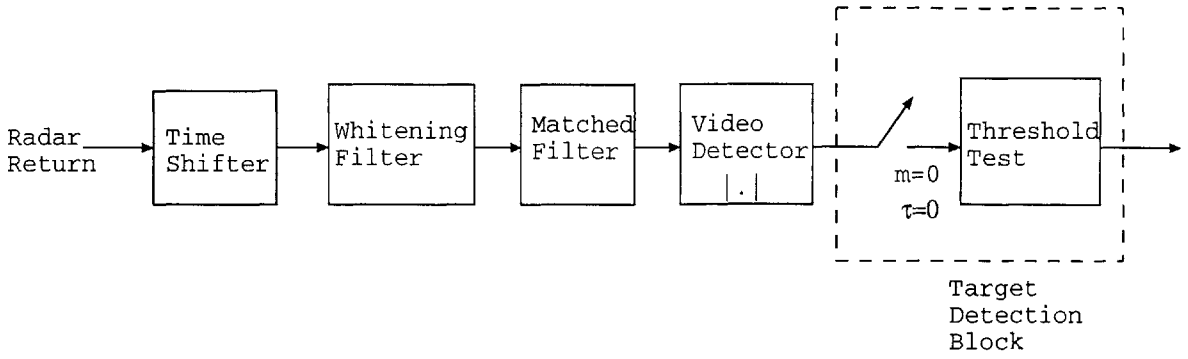

Figure 2-4: The whitening-filter optimum processor for detecting a single reflector at a known location

we can have a better idea about how far the adaptive-resolution processor's classification performance is from the ultimate theoretical limit. By comparing the performance of the optimized adaptive-resolution processor with its conventional-processor limit, we can learn how important it is to treat extended targets differently from point scatterers.

2.4 Multi-component Target Classification

A multi-component target is a collection of simple reflectors located at different positions. The radar-return signal from a multi-component target is the sum of the contributions from all its individual scatterers, because multiple scattering between different reflectors is neglected. A multi-component target classification problem is dealt with in the following manner. Let $\mathbf{s}(m, \tau)$ be the radar return from a multi-component target after passing through a whitening filter, thus, having the unwanted clutter-plus-noise component whitened to unity spectral density. We will use the boldface symbol to denote the fully polarimetric return signal (HH, VV, and HV where the vertical polarization aligns with an aircraft flight direction, $\hat{x}$ and horizontal polarization, with $\hat{y}'$, orthogonal to $\hat{x}$ and the antenna's nominal direction $\hat{z}'$). Then, if H_i denotes target i present among all N possible targets, $\mathbf{s}(m, \tau)$ can be written as

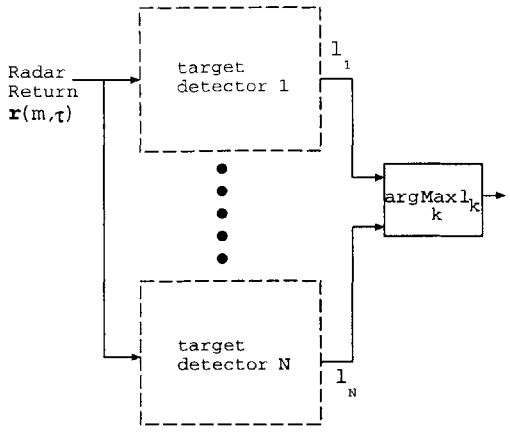

Figure 2-5: Block diagram of a multi-component target classifier. Each individual detector will depend on the specific target scenario.

follows:

$$\text{under } H_1: \quad \mathbf{s}(m,\tau) = \sum_{p^1=1}^{M_1} e^{i\phi_{p^1}} \mathbf{s}_{p^1}(m - m_{p^1}, \tau - \tau_{p^1}) + \mathbf{w}(m,\tau),$$

$$\vdots$$

$$\text{under } H_k: \quad \mathbf{s}(m,\tau) = \sum_{p^k=1}^{M_k} e^{i\phi_{p^k}} \mathbf{s}_{p^k}(m - m_{p^k}, \tau - \tau_{p^k}) + \mathbf{w}(m,\tau),$$

$$\vdots$$

$$\text{under } H_N: \quad \mathbf{s}(m,\tau) = \sum_{p^N=1}^{M_N} e^{i\phi_{p^N}} \mathbf{s}_{p^N}(m - m_{p^N}, \tau - \tau_{p^N}) + \mathbf{w}(m,\tau). \tag{2.1}$$

Here $\mathbf{w}(m,\tau)$ is the vector clutter-plus-noise complex envelope after the whitening filter. By construction it is white in the cross-range-time (m), range-time (τ) and polarimetric (vector) domains. Likewise, $\mathbf{s}_{p^k}(m_{p^k}, \tau_{p^k})$ corresponds to the post-whitening-filter radar-return complex envelope from the p-th component of the k-th

target when it is located at the scene center. The time delays m_{p^k}, τ_{p^k} for this component are determined by its actual location. The phases ϕ_{p^k} are independent random variables that are uniformly distributed within $[0, 2\pi)$; they represent the incoherence of each target-component with respect to other components as well as the noise. When the spatial separations between the individual target components are large enough, the following orthogonality condition will prevail:

$$\sum_m \int_{-\infty}^{\infty} d\tau \; \mathbf{s}_i^{\dagger}(m - m_i, \tau - \tau_i) \cdot \mathbf{s}_j(m - m_j, \tau - \tau_j) \approx 0 \tag{2.2}$$

for any two components located at different positions.

We can develop a target classifier for a repertoire of multi-component targets based on single-target detectors. Based on a maximum aposteriori probability (MAP) rule, a single-target detector can be constructed by passing the radar-return signal through a bank of matched filters (matched to each target reflector) and then combining filter outputs. Specifically, the likelihood ratio for a MAP target detector is

$$l_1(\mathbf{r}) = \frac{p_{\mathbf{r}|H_1}(r_1, r_2, ..., r_M|H_1)}{p_{\mathbf{r}|H_0}(r_1, r_2, ..., r_M|H_0)} = \prod_{m=1}^{M} \exp[-E_m] I_0(2|r_m|). \tag{2.3}$$

where hypothesis H_0 means target is absent, H_1 means target is present, E_m is the energy of the m-th component return, and I_0 is the zeroth-order modified Bessel function. $\mathbf{r}$ here is the vector of matched filter outputs sampled at the proper times; it has complete information about the whole radar return signal needed for the classification operation. At the output stage of a target detector, a real-valued level, which is equal or monotonically related to the likelihood ratio, is compared with a threshold level in order to decide on the absence or presence of that target. When there can be more than one possible target type, we can pass the radar return through a bank of target detectors, one for each target type. As in Figure 2-5 the resulting real-valued output levels l_1, ..., l_N are the likelihood ratios of conditions H_1, ..., H_N with respect to condition H_0 (clutter and noise only). To carry out classification, we select their maximum value; if the p-th detector has maximum output, then the classifier decides

the target to be type p.

The evaluation of multi-component target classification performance is computationally intensive, because the likelihood values of different multi-component targets will, in general, be correlated. Yeang presents the performance analysis for a specific target-repertoire example, in which upper and lower bounds on the probability of correct classification can be analytically obtained [10]. These bounds on PCC turn out to depend only on the signal-to-noise-plus-clutter ratio (SNCR) values for specular and dihedral reflectors, and, not surprisingly, turn out to decrease monotonically as the noise level increases.

A conventional SAR target classifier can be similarly constructed by paralleling the conventional SAR target detectors associated with the target types of concern. By following the procedures similar to those used in an optimum classifier, we also have an upper bound and a lower bound for the conventional SAR classifier's performance for the previous target setting.

Chapter 3

General Target Setting

3.1 Classification Scheme

It was noted that the computation of target classification performance is, in general, demanding due to the dense correlation between the likelihood values of different targets. Although Yeang's prior work has given preliminary bounds on PCC, it was limited to a specific target scenario in which the formulation for PCC can be significantly simplified. In addition, it was assumed that target component locations are known and known to satisfy an orthogonality condition. The rest of the thesis, hence, focus on the assessment of the comprehensive classification performance for a general target condition.

A general target setting, within the scope of this thesis, is one in which each target component can be located anywhere consistent with the orthogonality condition (2.2). For the PCC upper bound developed in section 3.2, and the PCC lower bound developed in section 3.3, the target components are assumed to be fixed at known positions, but the phase of the target signal from each component is randomly distributed in a uniform fashion. The random phase represents the unavailability of accurate relative phase information between the various components of a multi-reflector target. The radar return model under this target condition is specified by (2.1) and the time delays corresponding to the target component locations (m_{p^k}, τ_{p^k}) are presumed known. The block diagram of the likelihood-ratio target detector is

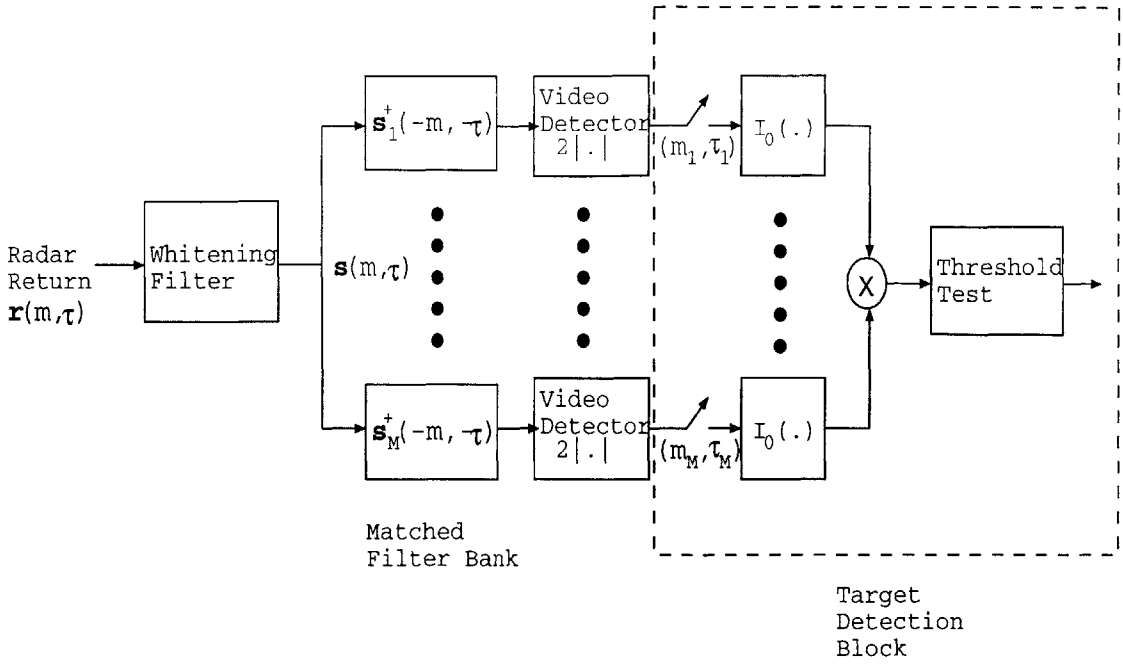

Figure 3-1: Block diagram of likelihood-ratio detector for the target with unknown phases

shown in Figure 3-1. To build a target classifier we employ a bank of likelihood-ratio (LR) detectors with one slight modification. After each Bessel function operation in a target detector, we need to normalize the output value by $\exp(-E_{p^i})$ where E_{p^i} is the output energy of target i's component p^i. The product of the normalized output values is a likelihood ratio, l_i, of condition H_i with respect to condition H_0. To carry out classification, we do not pass the $\{l_k\}$ through individual threshold comparators, but select their maximum value.

3.2 Upper Bound on PCC

Obtaining an upper bound on PCC is equivalent to finding a lower bound on error probability. If component phase information were exactly known and optimally employed, error probability will not be any higher than when the component phases are random. Given exact phases, the classification problem simply becomes M-ary detection of signals in an additive Gaussian noise channel. In general the error probability for detection of M signals over the additive white Gaussian noise channel is not available in a closed form. Thus, we again use a lower bound on this error probability.

To get a lower bound on probability of error for M-ary signals with additive white Gaussian noise, one could simply take the maximum error probability for binary detection (3.5), but this tends to be a loose bound, especially when there are two or more relatively-similar signals:

$$\begin{aligned} \mathrm{PCC} &= \sum_{i=1}^{N} \mathrm{P}(\textit{say } H_j \mid H_i \textit{ true})\mathrm{P}(H_i) && (3.1)\\ &= \sum_{i=1}^{N} \{1 - \mathrm{P}(\textit{error} \mid H_i \textit{ true})\}\mathrm{P}(H_i) && (3.2) \end{aligned}$$

$$\begin{aligned} \mathrm{P}(\textit{error} \mid H_i \textit{ true}) &\geq \mathrm{P}(\textit{error} \mid H_i \textit{ true, phase information given}) && (3.3)\\ &= \mathrm{P}(\bigcup_{j\neq i} \mathcal{E}_{ij} \mid H_i \textit{ true, phase information given}) && (3.4)\\ &\geq \max_{j\neq i} \mathrm{P}(\mathcal{E}_{ij} \mid H_i \textit{ true, phase information given}) && (3.5) \end{aligned}$$

Here $\mathcal{E}_{ij} = \{\|\mathbf{r}' - \mathbf{s}_j\| \leq \|\mathbf{r}' - \mathbf{s}_i\|\}$ and $\mathbf{r}'$ is a matched-filter-output vector, matched to all distinct target-components, and properly normalized to make the noise part circulo-complex Gaussian with unit-variance. $\mathbf{s}_i$ is the mean of $\mathbf{r}$ when the target i is present. The prior probability of target i, $P(H_i)$, will be assumed to be $1/N$, i.e., all targets will be assumed equiprobable.

Instead of taking the maximum over all possible binary error probabilities, de Caen's inequality (3.6) can be used to get a tighter lower bound on the probability of a union.

de Caen's inequality:

$$\mathrm{P}(\bigcup_{j=1}^{N} A_j) \geq \sum_j \frac{\mathrm{P}(A_j)^2}{\sum_k \mathrm{P}(A_j \cap A_k)} \qquad (3.6)$$

Applying this inequality to the probability of error [13], we obtain

$$\mathrm{P}(\textit{error} \mid H_i \textit{ true}) \geq \sum_{j\neq i} \frac{Q^2(d_{ij}/2)}{\sum_{k\neq i} \Psi(\rho_{jk}, d_{ij}/2, d_{ik}/2)} \qquad (3.7)$$

where

$$d_{ij} = \|\mathbf{s}_i - \mathbf{s}_j\|,$$

$$\rho_{jk} = \frac{< \mathbf{s}_i - \mathbf{s}_j, \mathbf{s}_i - \mathbf{s}_k >}{\|\mathbf{s}_i - \mathbf{s}_j\|\|\mathbf{s}_i - \mathbf{s}_k\|},$$

$$Q(x) = \frac{1}{\sqrt{2\pi}} \int_x^\infty \exp(-y^2/2) dy,$$

$$\Psi(\rho_{jk}, d_{ij}/2, d_{ik}/2) = \frac{1}{2\pi\sqrt{1-\rho_{jk}^2}} \int_{d_{ij}/2}^\infty \int_{d_{ik}/2}^\infty \exp(-\frac{x^2 - 2\rho_{jk}xy + y^2}{2(1-\rho_{jk}^2)}) dx\, dy.$$

This inequality deals with only two joint Gaussian random variables, and we have all constants needed for the calculation, namely, the distances between all signal points. The error probability is, hence, easy and straightforward to calculate. It can be shown that this bound is almost always tighter than the maximum binary-error-probability bound for non-trivial cases.

This method of obtaining an upper bound on PCC can be applied to all processor models we are dealing with, namely, a conventional full-resolution imager, an adaptive-resolution imager, and a whitening filter processor, and to both operational modes, which are stripmap- and spotlight-mode.

3.3 Lower Bound on PCC

A lower bound on the PCC can be calculated by finding a PCC for any sub-optimal classifier. For a sub-optimal classifier, we will use a component-wise detection rule. Suppose that each component is orthogonal to the others, and that only two reflectors – specular and dihedral – are considered as valid reflectors. Then, we can decide either specular or dihedral reflector for each component separately, and use these component decisions as inputs to a (sub-optimum) maximum aposteriori probability (MAP) M-ary decision rule. We can view the decision for each target component as a binary discrete memoryless channel (DMC), with transition probabilities calculated from the model in Figure 3-2. Combining the transition probabilities of the DMC with an M-ary decision rule based on the DMC outputs, an error probability is then easily

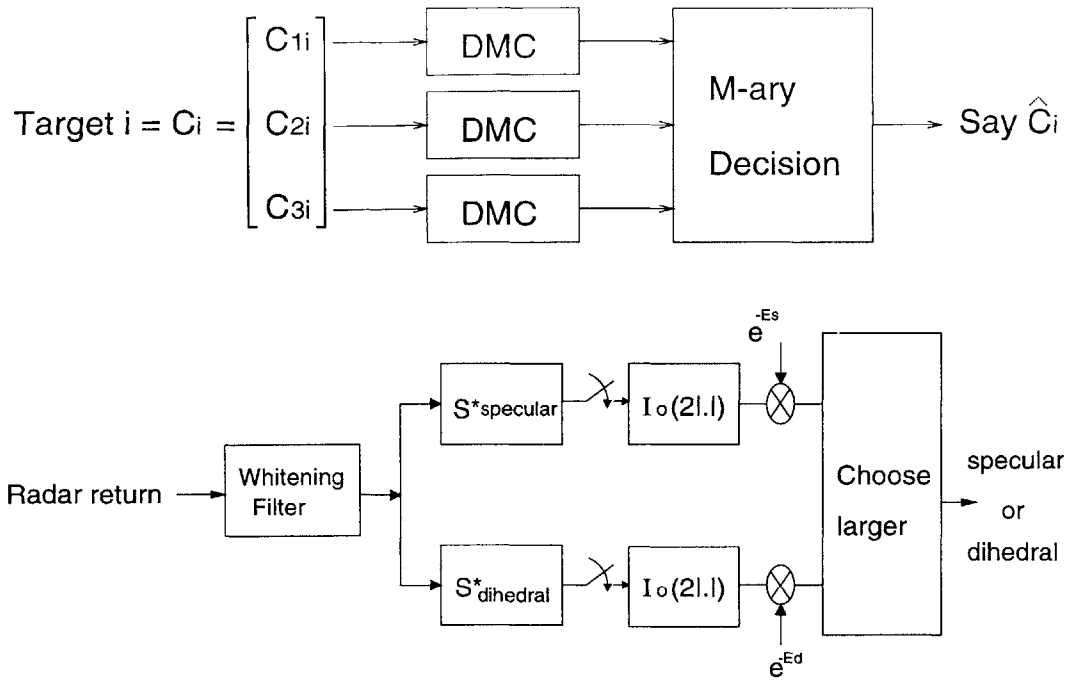

Figure 3-2: Upper panel represents a target classifier for three-component targets based on component-wise detection. Lower panel shows a model for a discrete memoryless channel.

calculated.

Like the upper bound on PCC previously presented, this lower bound can be applied to all processor models and both operation modes. However, for an operational mode we will only consider the spotlight-mode for our examples, because the change of modes does not affect our analysis of classification performance.

For the following example and on, we will use the radar geometries and parameters specified by Table 3.1. Although these parameters are not based on any real SAR imaging system, they are not far from the specification of such a system. Figure 3-3 compares the bounds on the PCC of the conventional classifier to those for the PCC of the optimal whitening-filter classifier for the particular 3-component target constellation in Table 3.2. PCC values are plotted with respect to clutter-to-noise ratio (CNR). The quantity 1/CNR measures the intensity of the noise with respect to a fixed clutter level. As the noise level increases, both lower bounds converge asymptotically to 1/3, which is a desirable result: when noise intensity is very high,

Flight Parameters	Radar Parameters	Reflector Parameters
aircraft altitude $L = 5000\,\mathrm{m}$	antenna radii $a_x = a_y = 1\,\mathrm{m}$	target radii $\rho_t = 1.5\,\mathrm{m}$
aircraft speed $v = 100\,\mathrm{m/s}$	Tx and LO powers $P_T = P_{LO} = 1\,\mathrm{W}$	relative permittivity $\epsilon_r = 10 + i5$
slant angle $\psi = 45°$	radar frequency $f_c = \Omega_c/2\pi = 10\,\mathrm{GHz}$	HV clutter strength $\epsilon = 0.2$
	pulse-repetition period $T_s = 10\,\mathrm{ms}$	HH×VV correlation $\rho = 0.57$
	pulse width $T_0 = 0.05\,\mu\mathrm{s}$	
	chirp bandwidth $W_0 = 100\,\mathrm{MHz}$	

Table 3.1: Parameter values for SNCR calculations

	Target 1	Target 2	Target 3
Component 1 type	specular	specular	specular
Component 1 (Δ_x, Δ_y)	(0 m, 0 m)	(0 m, 0 m)	(0 m, 0 m)
Component 1 orientation	0°	0°	0°
Component 2 type	specular	specular	dihedral
Component 2 (Δ_x, Δ_y)	(-7 m, -3 m)	(-7 m, -3 m)	(-7 m, -3 m)
Component 2 orientation	0°	0°	45°
Component 3 type	specular	dihedral	dihedral
Component 3 (Δ_x, Δ_y)	(5 m, -5 m)	(5 m, -5 m)	(5 m, -5 m)
Component 3 orientation	0°	45°	45°

Table 3.2: Specification of target constellation for the example in section 3.3. Notice the orientation angle of a specular reflector refers to the angle between the slant range and the normal direction of the plate, the orientation angle of a dihedral reflector means the angle between the SAR flight path direction and the dihedral axis. The side lengths, ρ_t, of all target components are 0.5 m.

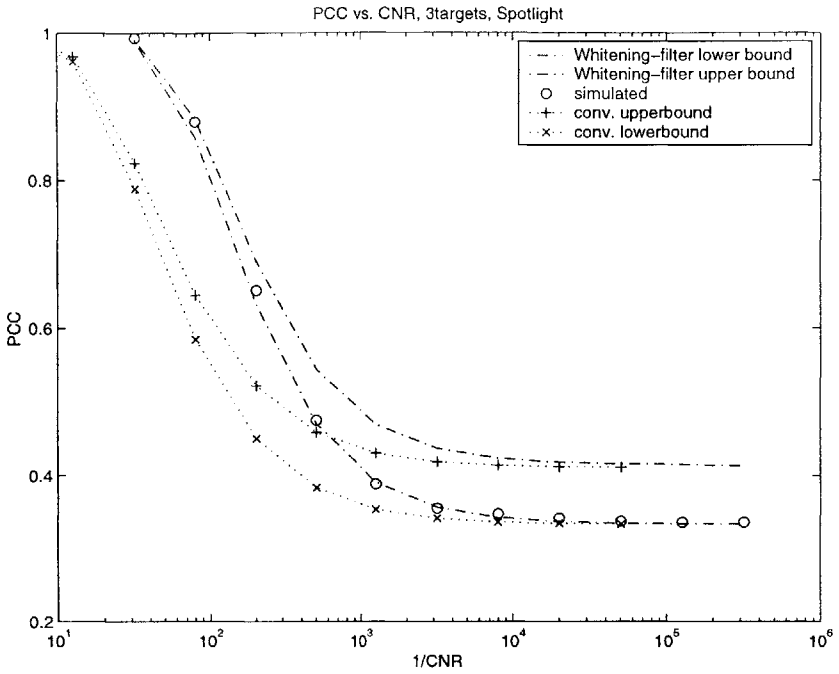

Figure 3-3: PCC for whitening filter processor and conventional processor

the classification operation simply becomes a blind guess. The PCC results from a 5000-trial computer simulation are also plotted. The simulation results turn out to be very close to the lower bound. We can see that the optimal classifier has about 6 dB of gain in terms of PCC. There are three factors that lead to the whitening-filter processor's performance advantage over the conventional SAR processor: the effect of the whitening filter, the polarimetric effect, and the adaptive-resolution effect. Since the conventional processor makes use of only single polarization (HH) whereas the whitening-filter processor takes full advantage of all polarimetric values, the whitening-filter processor enjoys a 3 dB enhancement of its SNCR value. The additional (approximately) 3dB gain of the whitening-filter processor comes from the adaptive-resolution effect and the whitening of clutter plus noise.

To highlight the difference between the PCC lower bound developed in this thesis and the one in previous work by Yeang [10], we first compare his PCC lower bound

for this example shown in Fig 3-3,

$$\text{PCC} \geq \frac{1}{3}(Q_1^2 + Q_1 Q_2 + Q_2^2). \tag{3.8}$$

to our PCC lower bound

$$\text{PCC} \geq \frac{1}{3}\{\max(Q_1^2, Q_2^2) + Q_1 Q_2 + \min(Q_1, Q_2)\}, \tag{3.9}$$

for this example. Here, $Q_1 \equiv \text{P}(\textit{say specular} \mid \textit{specular is true})$, and $Q_2 \equiv \text{P}(\textit{say dihedral} \mid \textit{dihedral is true})$ are the transition probabilities of the DMC. It is easy to note that the PCC lower bound developed in this thesis (3.9) is always tighter than the previous Yeang's lower bound (3.8). These PCC lower bounds are plotted in Figure 3-4 along with the Yeang's upper bound, our upper bound and results from a 5000-trial computer simulation. We see several things from Fig 3-4. First, the new lower bound (derived in this thesis) converges to the true PCC value of 1/3 as CNR $\rightarrow$ 0, whereas Yeang's lower bound is substantially lower in this high-noise regime. Second, Yeang's upper bound is tighter than the upper bound from this thesis. We must note, however, that Yeang's upper and lower bounds rely on special symmetries that are present in the example being considered here, whereas our bounds can be applied to any target setting which obeys the orthogonality condition. In a following example we will obtain lower and upper bounds on PCC of a whitening-filter-based classifier for a certain target component setting which can not be dealt with the previous approach.

3.4 Example

The upper and lower bound previously introduced can be readily applied to a general target structure. In this example, Target 1 has the three specular reflectors but Target 2 has a dihedral reflector and a specular reflector and Target 3 has two dihedral reflectors as specified by Table 3.3. For this target constellation, the computing of the probability of error by the direct evaluation, would be exorbitant because not all

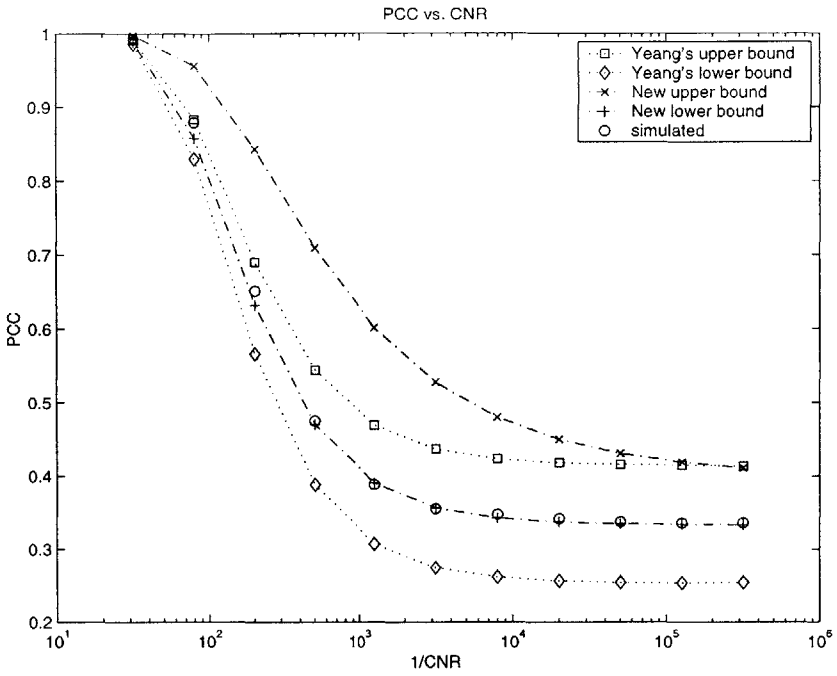

Figure 3-4: Yeang's PCC bounds and new bounds

targets share the same components, thus, making the computation of the probability of error involve high-dimensional integration. For a component-wise decision rule, a ternary discrete memoryless channel is employed to incorporate an additional "null" reflector. The detection scheme for three target reflectors is similar to that shown in Figure 3-2 except we have one additional value, 1 to be compared with the two other outputs from matched filters, i.e., those matched to the dihedral and specular reflectors.

The transition probabilities are easily calculated by similar fashion to that used in the binary case. Figure 3-5 plots the upper and lower bounds for the PCC and two versions of simulation with respect to 1/CNR using a whitening filter classifier. For the computer simulation, 5000 iterations were run.

We can observe the lower bound is very tight, compared to the simulation, and the upper bound is somewhat loose. By the proposed method of obtaining lower bound, we can now handle target setting where not all targets share the same reflectors,

	Target 1	Target 2	Target 3
Component 1 type	specular	dihedral	
Component 1 (Δ_x, Δ_y)	(0 m, 0 m)	(0 m, 0 m)	
Component 1 orientation	0°	0°	
Component 2 type	specular	specular	dihedral
Component 2 (Δ_x, Δ_y)	(-7 m, -3 m)	(-7 m, -3 m)	(-7 m, -3 m)
Component 2 orientation	0°	0°	45°
Component 3 type	specular		dihedral
Component 3 (Δ_x, Δ_y)	(5 m, -5 m)		(5 m, -5 m)
Component 3 orientation	0°		45°

Table 3.3: Specification of target constellation for the example in the section 3.4. The side lengths, ρ_t, of all target components are 0.5 m.

and the bound itself is very close to the true value. From the simulated result with known phases, compared to that with random phases, having exact phase information significantly improves classification performance in the intermediate noise strength regime.

Figure 3-6 plots the upper and lower bounds on PCC for the optimum processor and the lower bound for the conventional processor. We see that in the low noise region the optimal classifier has about 3 dB of gain in terms of PCC with respect to the conventional classifier.

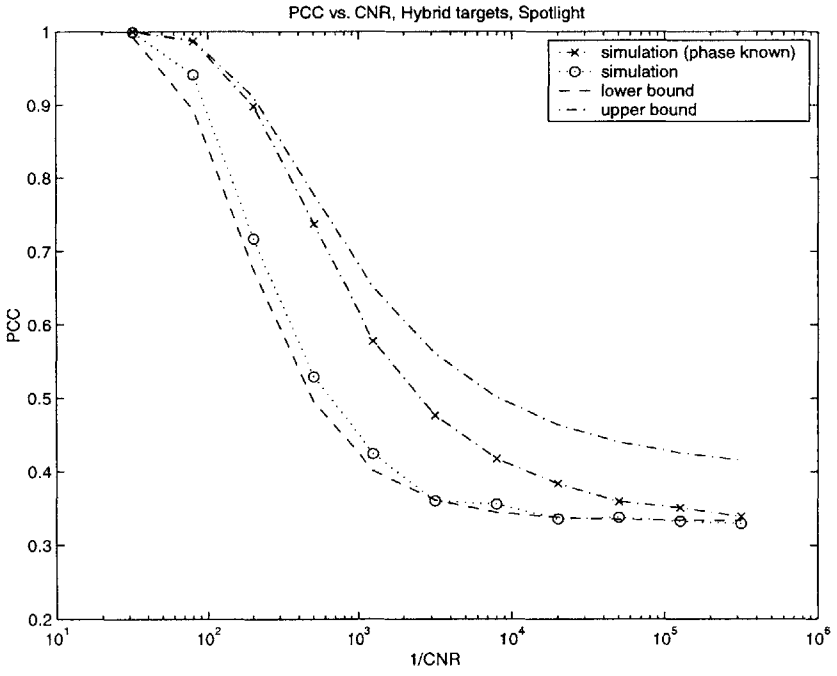

Figure 3-5: Lower, upper bounds on PCC for a complex target structure

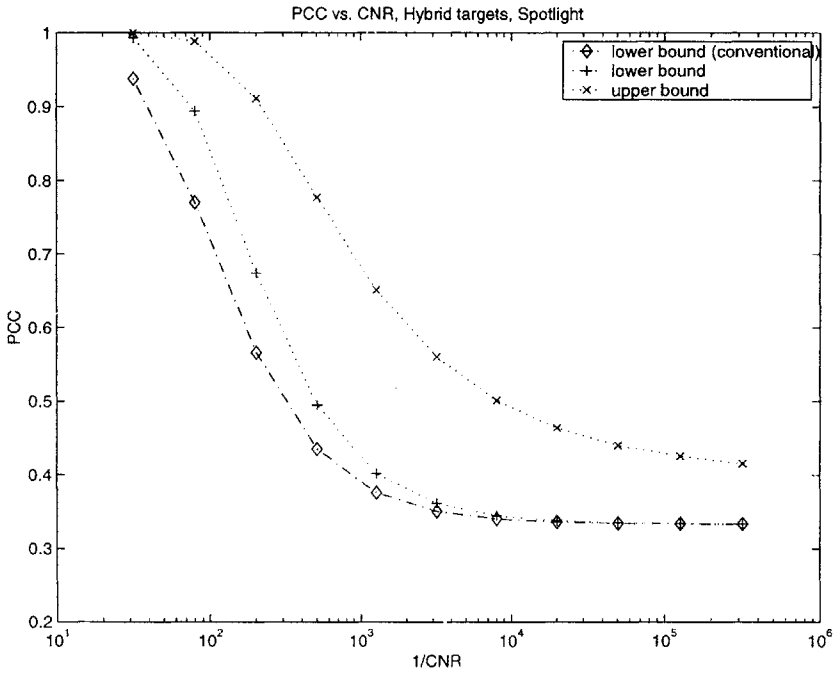

Figure 3-6: Lower, upper bounds on PCC for an optimum processor and PCC lower bound for a conventional processor

Chapter 4

Target with Unknown Positions

4.1 Classification Scheme

In this chapter, we will deal with the classification of targets with unknown reflector positions in addition to the uniform random phases of its reflector components. Incorporating the position uncertainty of the reflector components, the radar return for each hypothesis is modeled as follows:

$$\text{under } H_1: \quad \mathbf{s}(m,\tau) = \sum_{p^1=1}^{M_1} e^{i\phi_{p^1}} \mathbf{s}_{p^1}(m - m_{p^1}, \tau - \tau_{p^1}) + \mathbf{w}(m,\tau),$$

$$\vdots$$

$$\text{under } H_k: \quad \mathbf{s}(m,\tau) = \sum_{p^k=1}^{M_k} e^{i\phi_{p^k}} \mathbf{s}_{p^k}(m - m_{p^k}, \tau - \tau_{p^k}) + \mathbf{w}(m,\tau),$$

$$\vdots$$

$$\text{under } H_N: \quad \mathbf{s}(m,\tau) = \sum_{p^N=1}^{M_N} e^{i\phi_{p^N}} \mathbf{s}_{p^N}(m - m_{p^N}, \tau - \tau_{p^N}) + \mathbf{w}(m,\tau). \tag{4.1}$$

This is the same model as (2.1) except the center locations $(m_{p^k},\ \tau_{p^k})$ of the target components are no longer fixed and known to us. The random variables m_{p^k},

τ_{p^k} are assumed to be mutually independent and each random variable is uniformly distributed within $[m^0_{p^k} - M_{p^k}/2, m^0_{p^k} + M_{p^k}/2]$ for m_{p^k} and $[\tau^0_{p^k} - T_{p^k}/2, \tau^0_{p^k} + T_{p^k}/2]$ for τ_{p^k}. The position randomness models the variability or unavailability of exact knowledge about some aspects of a real-world target reflector constellation.

Because the delay times in (4.1) are uniform random variables, it is difficult to write down the likelihood ratio of two different hypotheses. We can, however, formulate the generalized likelihood ratio and develop a target classifier on that basis. For a specific realization of the delay times, one can formulate the likelihood ratio of hypotheses H_k (target k) with respect to the null hypotheses H_0 (clutter plus noise only):

$$\begin{aligned} & l_k(\mathbf{r}; m_1, ..., m_{M_k}, \tau_1, ..., \tau_{M_k}) \\ &= \frac{p_{\mathbf{r}|H_k}(r_1, r_2, ..., r_{M_k}|H_k; m_1, ..., m_{p^k}, \tau_1, ..., \tau_{M_k})}{p_{\mathbf{r}|H_0}(r_1, r_2, ..., r_{M_k}|H_0; m_1, ..., m_{p^k}, \tau_1, ..., \tau_{M_k})} \\ &= \prod_{p^k=1}^{M_k} \exp\left[-\sum_m \int_{-\infty}^{\infty} d\tau s^*_{p^k}(m,\tau) \cdot s_{p^k}(m,\tau)\right] \\ &\quad \times I_0\left(2\left|\sum_m \int_{-\infty}^{\infty} d\tau s^*_{p^k}(m - m_{p^k}, \tau - \tau_{p^k}) \cdot r(m,\tau)\right|\right). \end{aligned} \tag{4.2}$$

For a given radar return $r(m,\tau)$, the likelihood ratio is a function of m_1,...,m_{M_k},τ_1,...,τ_{M_k}. One can obtain the maximum-likelihood estimate of these parameters from the radar return:

$$\begin{aligned} \begin{bmatrix} \hat{m}_1 \\ \vdots \\ \hat{m}_{M_k} \\ \hat{\tau}_1 \\ \vdots \\ \hat{\tau}_{M_k} \end{bmatrix} &= \arg \max_{m_1 \in [m^0_1 - M_1/2, m^0_1 + M_1/2], ..., \tau_1 \in [\tau^0_1 - T_1/2, \tau^0_1 + T_1/2], ..} \\ & \prod_{p^k=1}^{M_k} \exp\left[-\sum_m \int_{-\infty}^{\infty} d\tau s^*_{p^k}(m,\tau) \cdot s_{p^k}(m,\tau)\right] \\ & \times I_0\left(2\left|\sum_m \int_{-\infty}^{\infty} d\tau s^*_{p^k}(m - m_{p^k}, \tau - \tau_{p^k}) \cdot r(m,\tau)\right|\right) \end{aligned} \tag{4.3}$$

where $\hat{m}_1$, ..., $\hat{m}_{M_k}$, $\hat{\tau}_1$, ..., $\hat{\tau}_{M_k}$ are the maximum-likelihood estimates. The generalized likelihood ratio is defined as the likelihood ratio when the maximum-likelihood estimates as though they were the true values of the unknown parameters. Plugging (4.3) into (4.2), we have that:

$$\begin{aligned} \text{GLR} &= l_k(\mathbf{r}; \hat{m}_1, ..., \hat{m}_{M_k}, \hat{\tau}_1, ..., \hat{\tau}_{M_k}) \\ &= \max \prod_{p^k=1}^{M_k} \exp\left[-\sum_m \int_{-\infty}^{\infty} d\tau s_{p^k}^*(m,\tau) \cdot s_{p^k}(m,\tau)\right] \\ &\quad \times I_0\left(2\left|\sum_m \int_{-\infty}^{\infty} d\tau s_{p^k}^*(m - m_{p^k}, \tau - \tau_{p^k}) \cdot r(m,\tau)\right|\right) \end{aligned} \tag{4.4}$$

where the maximum is over $m_1 \in [m_1^0 - M_1/2, m_1^0 + M_1/2], ..., m_{M_k} \in [m_{M_k}^0 - M_{M_k}/2, m_{M_k}^0 + M_{M_k}/2]$ and $\tau_1 \in [\tau_1^0 - T_1/2, \tau_1^0 + T_1/2], ..., \tau_{M_k} \in [\tau_{M_k}^0 - T_{M_k}/2, \tau_{M_k}^0 + T_{M_k}/2]$. The generalized-likelihood-ratio detector based on (4.4) can be written in the following form:

$$\max \prod_{p^k=1}^{M_k} \left[I_0\left(2\left|\sum_m \int_{-\infty}^{\infty} d\tau s_{p^k}^*(m - m_{p^k}, \tau - \tau_{p^k}) \cdot r(m,\tau)\right|\right)\right] \begin{array}{c} \text{say } H_k \\ > \\ < \\ \text{say } H_0 \end{array} \beta \tag{4.5}$$

where β is the threshold and the maximum is over the same domain as in (4.4). Furthermore, since the zeroth-order modified Bessel function is monotonically increasing and m_1, ..., m_{M_k}, τ_1, ..., τ_{M_k} are mutually independent variables, maximizing the overall product of I_0's in (4.5) is equivalent to maximizing the individual I_0's in the product. Hence the generalized-likelihood-ratio detector becomes

$$\prod_{p^k=1}^{M_k} \max \left[I_0\left(2\left|\sum_m \int_{-\infty}^{\infty} d\tau s_{p^k}^*(m - m_{p^k}, \tau - \tau_{p^k}) \cdot r(m,\tau)\right|\right)\right] \begin{array}{c} \text{say } H_k \\ > \\ < \\ \text{say } H_0 \end{array} \beta \tag{4.6}$$

The form of the GLR detector is similar to the LR detector discussed in the

previous chapter except that in the GLR detector the value used to compare the threshold is maximized over the region of delay-time uncertainty. This operation can be achieved by inserting a duration-limited peak detector after video detection of the output from each individual matched filter. Figure 4-1 sketches the block diagram of the generalized-likelihood-ratio detector. A target classifier can be built as discussed in the previous chapter, by employing a bank of target detectors, incorporating the energy corrections, and choosing the largest output level.

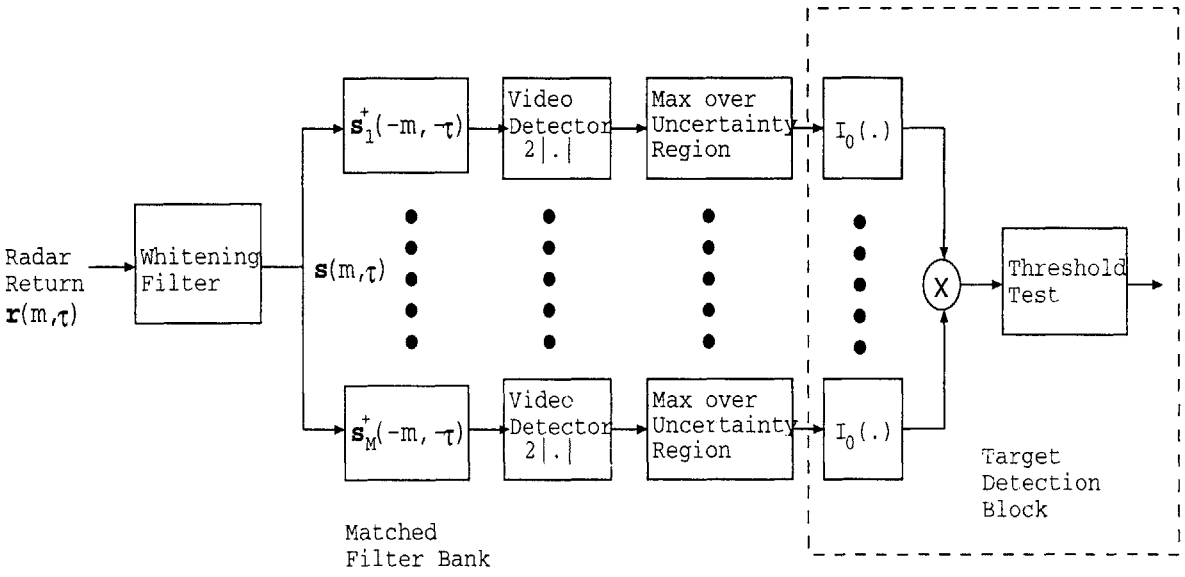

Figure 4-1: Block diagram of generalized-likelihood-ratio detector for the target with unknown phases and positions

In order to calculate PCC for the M-ary target recognition problem, we need to obtain the statistical structure of the generalized likelihood ratio, as will become more evident later in this chapter. As implied by (4.6), to obtain the statistics of the GLR we must solve the following general level-crossing problem: for a complex 2-D random process with a given covariance function and a fixed real-valued threshold level, what is the probability that this random process is smaller than the threshold level within a given area. When the target is absent or all its components are mismatched to the detector's filters, then this random process is approximately stationary; when at least one of the target components is matched to the detector's filters, this process is

non-stationary. As a result we ought to consider the level-crossing problems for H_0 and H_k ($k \neq 0$) separately.

4.2 Level Crossing Theory

Since the level-crossing theory for a 1-D stationary random process has been actively studied, we will begin with 1-D level crossing theory, and then extend the result to the 2-D case which we need for our PCC analysis. The problem is to obtain an analytic form of following probability: for a real 1-D random process $r(t)$ with a given covariance function $u(t)$ and a fixed threshold level a, what is the probability, $P(T; a)$, that $r(t)$ is smaller than a for all the t within $[0, T]$. For a real Markov process or a complex-valued Gauss-Markov process with mutually independent real and imaginary parts, analytical expressions for the level crossing probability can be obtained from Siegert's theory [14] [15]. However, in general the analytical solution for the level crossing probability of a non-Markov stationary process is not available. Among a few possible methods of obtaining the approximate form of this probability, we will use the resolution-bin model.

In the laser radar literature, it is a common practice to apply the resolution-bin model to calculate level-crossing probabilities [16]. The basic idea is to divide the interval of concern, $[0, T]$, into a sequence of N resolution bins with center locations t_1, t_2, ..., t_N, where the bin size is on the order of the correlation time for the random process under consideration. Then it is reasonable to approximate the probability that the real random process $r(t)$ is smaller than a within the whole interval $[0, T]$ by the joint probability that $r(t_1) < a$, $r(t_2) < a$, ..., and $r(t_N) < a$. Furthermore, if the bin size is not significantly smaller than the correlation length, then the random variables $r(t_1)$, $r(t_2)$, ..., $r(t_N)$ can be taken, approximately, to be statistically independent. The joint level-crossing probability is then the product of level-crossing probabilities for each individual sample point. For a stationary random process, $r(t_1)$, $r(t_2)$, ..., and $r(t_N)$ have the same probability density function. The resulting joint level-crossing probability is then the N^{th} power of a sample point's level-crossing probability. In

other words,

$$P(T;a) = \Pr\{r(t) < a; 0 \le t \le T\} \approx \Pr\{r(t_1) < a \ \& \ r(t_2) < a \ \& \ .... \ \& \ r(t_N) < a\}$$

$$\approx \prod_{i=1}^{N} \Pr\{r(t_i) < a\} = [\Pr\{r(t_i) < a\}]^N. \tag{4.7}$$

For a zero-mean circulo-complex Gaussian process $z(t)$ with covariance function $u(t)$, the approximate probability $P(T;a)$ that $|z(t)| < a$ within $[0,T]$ can also be obtained from the resolution bin model via (5.48). To calculate the probability that $|z(t_i)| < a$, the chi-squared distribution is applied. The result for the probability $P(T;a)$ is

$$P(T;a) \approx \{1 - \exp\left[-\frac{a^2}{u(0)}\right]\}^{T/t_{bin}}, \tag{4.8}$$

where t_{bin} is the bin duration.

If we extend the 1-D resolution-bin model to the 2-D case, we find that:

$$P(X,Y;a) \approx \{1 - \exp\left[-\frac{a^2}{u(0,0)}\right]\}^{XY/x_{bin}y_{bin}} \tag{4.9}$$

is the probability that a zero-mean circulo-complex Gaussian random process, $z(x,y)$, will satisfy $|z(x,y)| < a$ for $0 \le x \le X$ and $0 \le y \le Y$. Here, x_{bin} and y_{bin} are bin sizes along the x and y directions, and $u(x,y)$ is the 2-D covariance function of $z(x,y)$.

4.3 Lower bound on PCC

Paralleling the work in the last chapter, a component-wise detector can be exploited to obtain a lower bound on PCC for the random position case. Any sub-optimal classifier will be inferior in its classification performance to an optimum one. Thus, the PCC for a sub-optimal target recognizer is a valid PCC lower bound for an optimum classifier. Figure 4-2 depicts the block diagram of a component-wise detector. This detector can be seen as an optimum target detector for two targets with single reflector (specular or dihedral). We do a binary detection for each reflector component,

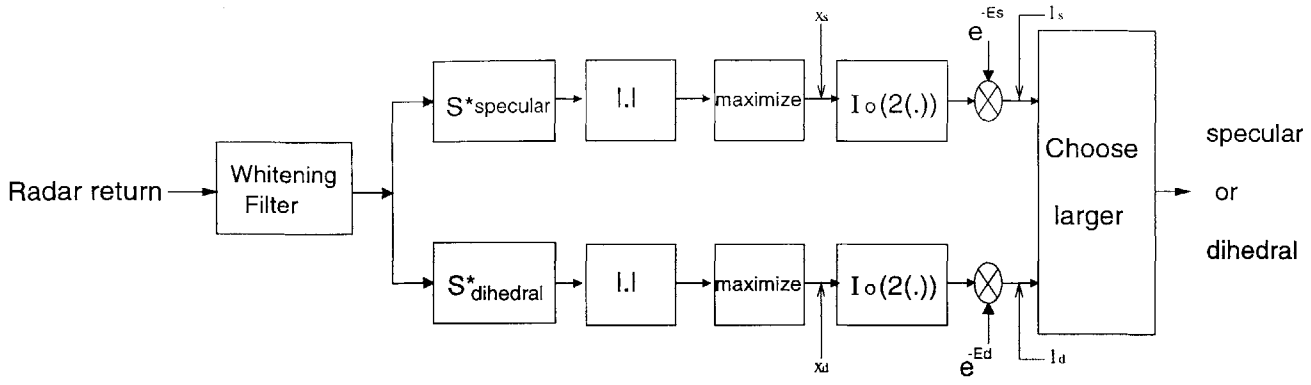

Figure 4-2: Block diagram of component-wise detector

gather results from each component-wise detectors to make maximum aposteriori probability M-ary decision. This is a valid classification scheme but not necessarily an optimum one. For our general target setting, the component-wise detector incorporates a null reflector by choosing the largest output among l_s (specular), l_d (dihedral) and 1 (no reflector). To obtain PCC for this sub-optimal classifier, we only need to know the transition probabilities for the component-wise detector. Let's assume the true target component is specular and find the transition probability, $Q_1 \equiv \mathrm{P}(\textit{say specular} \mid \textit{specular is true})$.

$$
\begin{aligned}
Q_1 &= \mathrm{P}[l_s > l_d \mid \text{specular}] && (4.10)\\
&= \mathrm{P}[I_0(2x_s)e^{-E_s} > I_0(2x_d)e^{-E_d} \mid \text{specular}] && (4.11)\\
&= \mathrm{P}[x_s > \frac{1}{2}I_0^{-1}(e^{E_s-E_d}I_0(2x_d)) \mid \text{specular}] && (4.12)\\
&= 1 - \mathrm{P}[x_s < \frac{1}{2}I_0^{-1}(e^{E_s-E_d}I_0(2x_d)) \mid \text{specular}] && (4.13)\\
&= 1 - \int_0^\infty dX_d p_{x_d|\text{specular}}(X_d|\text{specular})\mathrm{P}[x_s < \gamma \mid \text{specular}] && (4.14)
\end{aligned}
$$

where $\gamma = \frac{1}{2}I_0^{-1}(e^{E_s-E_d}I_0(2X_d))$.

To evaluate the last term, we need to know the probability structure of x_s and x_d. We treat $p(x_s \mid \text{specular})$ and $p(x_d \mid \text{specular})$ separately since their statistical behaviors are quite different. For x_s, the radar return is passed through a filter which is matched to that of the specular return signal. The maximization process

will pick up the peak value of the magnitude of post-matched-filter signal within the uncertainty region. If we chop up the uncertainty region into resolution bins and assume that each bin is statistically independent of the others, we can formulate the cumulative distribution function of x_s as follows:

$$\mathrm{P}[x_s < \gamma \mid \text{specular}] = P_1^{N-1}(\gamma) P_2(\gamma) \tag{4.15}$$

where N is the number of bins, $\mathrm{P}_1(\gamma)$ is the probability that the magnitude of stationary and noisy signal is always less than γ for a given bin area, and $\mathrm{P}_2(\gamma)$ is the cumulative distribution function (CDF) of the output value from a perfectly matched signal sampled at the correct position. $\mathrm{P}_1(\gamma)$ can be calculated by applying 2-D level-crossing theory, and $\mathrm{P}_2(\gamma)$ can be obtained analytically.

Now as for x_d, this is the case in which the radar return from a specular reflector is matched to dihedral signal. Thus, x_d will be stationary over the whole uncertainty region. We can, again, apply 2-D level crossing theory to obtain the CDF of x_d. Since we know the statistics of x_s and x_d, we can now evaluate the transition probability Q_1:

$$\begin{aligned} Q_1 &= 1 - \int_0^\infty dX_d p_{x_d|\text{specular}}(X_d|\text{specular}) \mathrm{P}[x_s < \gamma \mid \text{specular}] && (4.16) \\ &= 1 - \int_0^\infty dX_d p_{x_d|\text{specular}}(X_d|\text{specular}) P_1^{N-1}(\gamma) P_2(\gamma) && (4.17) \end{aligned}$$

$Q_2 \equiv \mathrm{P}(\textit{say dihedral} \mid \textit{dihedral is true})$ can be calculated in a similar way. Having both the transition probabilities, Q_1 and Q_2, we can make a M-ary decision based on MAP rule and obtain our component-wise lower bound on PCC for the case of position uncertainty.

4.4 Upper bound on PCC

To get an upper bound on PCC we assume that we have the exact phase information. Since this means we have more information for the classification task, the PCC for

the optimum receiver for this case will be a valid upper bound on PCC for the random phase case which we are interested in. If we assume all target components are orthogonal, we can set the phases to be zero for all target component signals without loss of generality. The radar return signal for each target is now formulated as follows:

$$\text{under } H_1: \quad \mathbf{s}(m,\tau) = \sum_{p^1=1}^{M_1} \mathbf{s}_{p^1}(m - m_{p^1}, \tau - \tau_{p^1}) + \mathbf{w}(m,\tau),$$

$$\vdots$$

$$\text{under } H_k: \quad \mathbf{s}(m,\tau) = \sum_{p^k=1}^{M_k} \mathbf{s}_{p^k}(m - m_{p^k}, \tau - \tau_{p^k}) + \mathbf{w}(m,\tau),$$

$$\vdots$$

$$\text{under } H_N: \quad \mathbf{s}(m,\tau) = \sum_{p^N=1}^{M_N} \mathbf{s}_{p^N}(m - m_{p^N}, \tau - \tau_{p^N}) + \mathbf{w}(m,\tau). \tag{4.18}$$

Using this return signal model, the likelihood ratio for the target k with respect to target 0 (the null hypothesis) is:

$$l_k(\mathbf{r}; m_1, ..., m_{M_k}, \tau_1, ..., \tau_{M_k})$$

$$= \prod_{p^k=1}^{M_k} \exp\left(-E_{p^k} + 2\Re\{\sum_m \int_{-\infty}^{\infty} d\tau s^*_{p^k}(m - m_{p^k}, \tau - \tau_{p^k}) \cdot r(m,\tau)\}\right). \tag{4.19}$$

where E_{p^k} is the energy of p^kth component of kth target. It is similar to (4.2) but does not involve a Bessel function. The generalized log likelihood ratio (GLLR) for the target k is expressed as:

$$\text{GLLR}_k \tag{4.20}$$

$$= \sum_{p^k=1}^{M_k} \exp\left(-E_{p^k} + 2\max\Re\{\sum_m \int_{-\infty}^{\infty} d\tau s^*_{p^k}(m - m_{p^k}, \tau - \tau_{p^k}) \cdot r(m,\tau)\}\right) \tag{4.21}$$

$$= \sum_{p^k=1}^{M_k} \exp\left(-E_{p^k} + 2y_{p^k}\right). \tag{4.22}$$

Here the statistics of y_{p^k} are easily calculated via level crossing theory. The probability of correct classification can be, then, evaluated as:

$$\begin{aligned}
\mathrm{PCC}|H_i &= 1 - \mathrm{P}(error \mid H_i \text{ is true}) && (4.23)\\
&\leq 1 - \mathrm{P}(error \mid H_i \text{ is true, phase information given}) && (4.24)\\
&= 1 - \mathrm{P}(\bigcup_{\forall j \neq i} \mathrm{GLLR}_i < \mathrm{GLLR}_j \mid H_i \text{ is true, phase info given}) && (4.25)\\
&\leq 1 - \max_{j \neq i} \mathrm{P}(\mathrm{GLLR}_i < \mathrm{GLLR}_j \mid H_i \text{ is true, phase info given}) && (4.26)
\end{aligned}$$

In the previous chapter we used de Caen's inequality (3.6) to obtain a tighter lower bound on the probability of a union, which involves the joint probability distribution of two Gaussian random variables. However, for this target setting, we can not apply de Caen's inequality in (4.26) because the statistics of GLLR_i are complicated. (4.26) can be calculated in a straightforward way since we have statistics for GLLR's.

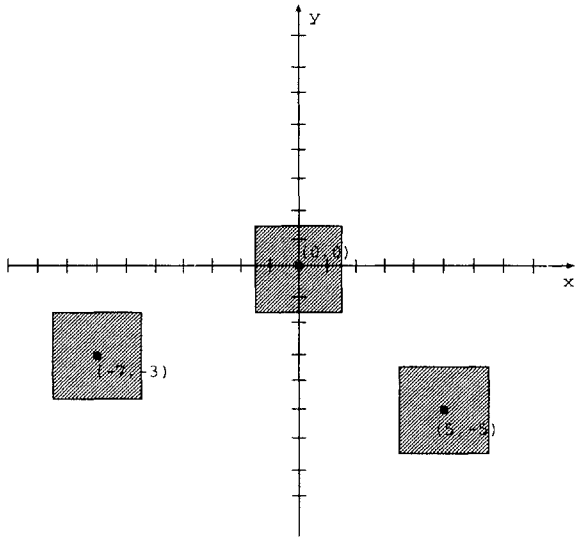

Figure 4-3: Specifications for the uncertainty-region geometries. Notice that $(0,0)$ is the scene center of the antenna footprint area. The aircraft flies along the x direction.

Since we have analytic forms available for both the lower and upper bounds developed in this chapter, a specific example is presented here. Figure 4-3 illustrates the uncertainty-region geometries for the example. The center locations for the target components are shown as dots, and (uniformly distributed) uncertainty regions are rendered shaded. The target component structures are the same as in Table 3.3. In Figure 4-4, PCC upper, lower bounds and simulation are plotted versus 1/(clutter-to-noise ratio). For the simulation, we generated random variables (x_s and x_d) according to the statistics discussed in the previous section, then used an optimum classifier based on the whitening-filter processor, that is, a bank of generalized-likelihood-ratio detectors (Figure 4-1). 100000 trials were performed for the simulation. The lower bound calculated with the given data, showed an anomalous feature: it was not monotonically decreasing in the high noise region. We believe that this anomaly was due to numerical errors, so we corrected our lower bound by extending the lowest PCC value to the higher noise region. The upper and lower bounds decrease asymptotically to one third as the noise (1/CNR) level increases. This is a desirable feature for the PCC bounds, because when the noise level is very high, classification is no better than a blind guess. We can observe that the lower bound is close to the simulation over the entire CNR region shown. The upper bound is generally somewhat loose compared to the lower bound, but is tight in the low-noise region. Figure 4-5 compares the lower/upper bounds for the unknown-position case to those for known-position case. Exact position information is seen to have the effect of about a 3 to 10 dB decrease in noise level.

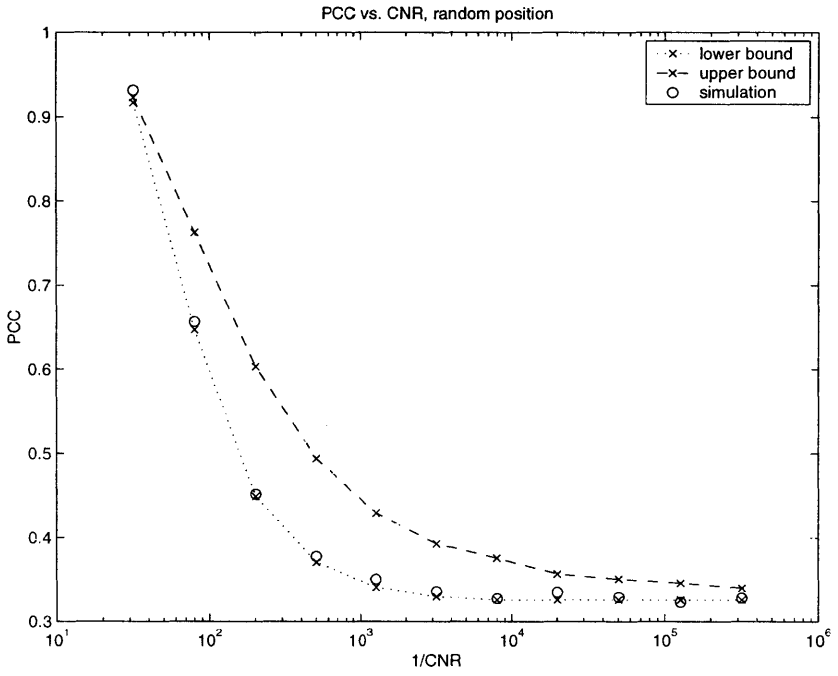

Figure 4-4: Lower and upper bounds on PCC for target components with unknown positions

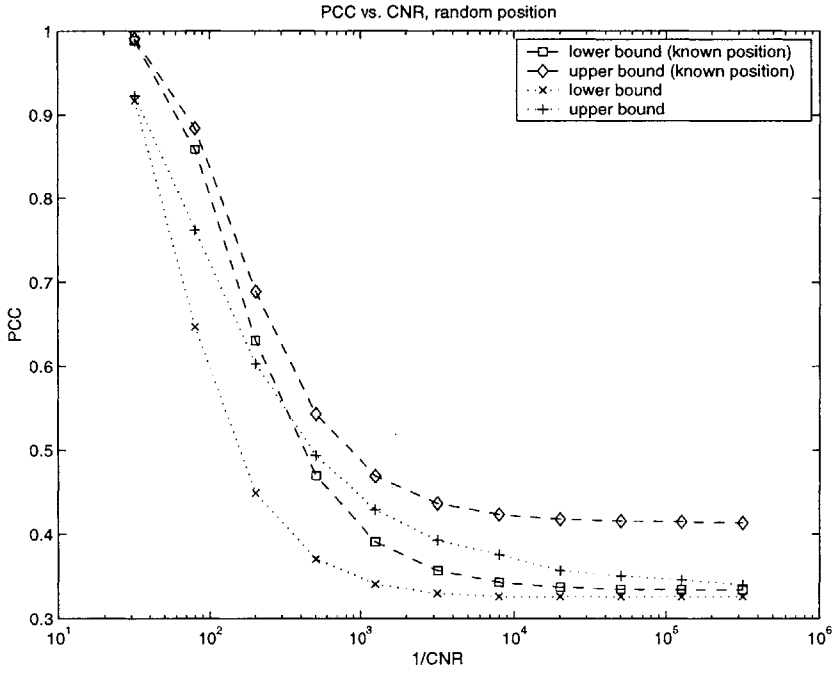

Figure 4-5: Lower and upper bounds on PCC for unknown positions compared to those for known positions

Chapter 5

Target with Unknown Pose

In this chapter we will deal with the classification performance assessment for targets with random pose. In this setting, the individual target components rotate around a pose center on the ground with a common random rotational angle.

5.1 Laplace Method

Thus far, we have done classification tasks based on a (generalized) likelihood-ratio test. The statistical structure of the necessary likelihood ratios were either available or approximated for the target conditions in the last chapters. For the targets with unknown pose that we are discussing in this chapter, although it is possible to obtain likelihood ratios in closed form, they will depend on the rotational angle, making the evaluation of PCC based on them unwieldy. Hence we turn to another approach to evaluate the classification performance.

The likelihood ratios involve the pose angle, and integration over pose angle is cumbersome and, in general, obtainable only by numerical methods. The Laplace method can be used for evaluating integrals for Bayesian inference [17] in the high signal-to-noise ratio (SNR) regime. The Laplace method is useful for calculating integrals of the form:

$$F(\sigma^2) = \int_{\theta_{min}}^{\theta_{max}} g(\theta) \exp(-\frac{h(\theta)}{2\sigma^2}) d\theta \tag{5.1}$$

which often appear in the likelihood expressions needed to evaluate the Bayesian decision rule. If $h(\theta)$ is positive in the interval $[\theta_{min}, \theta_{max}]$, then we can use the Laplace approximation to asymptotically evaluate $F(\sigma^2)$ in the limits $\sigma^2 \to 0$. The idea behind the approximation is that most of the integral is contained in a neighborhood of the θ value where $h(\theta)$ is a minimum, $\theta_0 \equiv \arg\min_\theta h(\theta)$. If we replace $h(\theta)$ with a two-term Taylor-series expansion about $\theta = \theta_0$, we have the Laplace-method approximation:

$$F(\sigma^2) \approx g(\theta_0) \exp(-\frac{h(\theta_0)}{2\sigma^2}) \sqrt{\frac{4\pi\sigma^2}{h''(\theta_i)}}, \text{ as } \sigma^2 \to 0. \tag{5.2}$$

In [18], the single-pixel return signal from a forward-looking infrared (FLIR) intensity image is modeled as $x_{ij}(\theta) = x^*_{ij}(\theta) + n_{ij}$, where $x^*_{ij}(\theta)$ is the noise-free value at the target orientation angle θ and n_{ij} is a zero-mean unity-variance Gaussian random variable. It turns out that the distance measure between two targets ($k = 1, 2$), $E_k(\theta, \theta_1) \equiv \sum_{i,j}(x_{k,ij}(\theta) - x_{1,ij}(\theta_1))^2$ plays a key role in calculating the probability of detection/recognition error via the Laplace method. Specifically, when the true target is fixed as H_1 at true pose θ_1, the conditional probability of error $\mathrm{P}(e|H_1, \theta_1)$ is approximated by:

$$\mathrm{P}(e|H_1, \theta_1) \approx Q(\kappa) = \int_\kappa^\infty \frac{\exp(-t^2/2)}{\sqrt{2\pi}} dt \tag{5.3}$$

where

$$\kappa = \frac{D}{2\sigma} - \frac{\sigma}{2D} \log \frac{\ddot{E}_1(\theta_1)}{\ddot{E}_2(c)}.$$

The error probability only depends on κ value and is monotonically decreasing as κ increases. The parameters we need to obtain in order to calculate κ, thus the error probability are:

$$D = \min_\theta \|\mathbf{x}_2(\theta) - \mathbf{x}_1(\theta_1)\|, \tag{5.4}$$

$$\ddot{E}_1(\theta_1) = \left. \frac{\partial^2 \|\mathbf{x}_1(\theta) - \mathbf{x}_1(\theta_1)\|^2}{\partial\theta^2} \right|_{\theta=\theta_1}, \tag{5.5}$$

$$\ddot{E}_2(c) = \left.\frac{\partial^2 \|\mathbf{x}_2(\theta) - \mathbf{x}_1(\theta_1)\|^2}{\partial\theta^2}\right|_{\theta=c}, \tag{5.6}$$

$$c = \arg\min_{\theta} \|\mathbf{x}_2(\theta) - \mathbf{x}_1(\theta_1)\|. \tag{5.7}$$

5.2 Conditional Probability of Error

For this section, we restrict the true target to be H_1 at pose θ_1. Previous work, via electromagnetic theory [10], modeled the raw SAR return signal from specular reflector as follows:

$$\mathbf{r}(m,\tau;\theta)_{\text{specular}} \approx -\frac{\sqrt{P_T P_{LO}}\Omega_c^2 a_x a_y}{2\pi c^2 L'^2} 4{\rho_t}^2 (\hat{z}' \cdot \hat{n}_{sb}) \exp(-4(\tau - \Delta_\tau)^2/T_0^2)$$

$$\times \text{sinc}[\Omega_c \alpha_{xb}(\theta)\rho_t/c]\ \text{sinc}[\Omega_c \alpha_{yb}(\theta)\rho_t/c] \begin{bmatrix} 1 \\ 1 \\ 0 \end{bmatrix}. \tag{5.8}$$

where

$$\alpha_{xb}(\theta) = -\frac{2(mvT_s - \Delta_x)}{L'} \sin(\phi_{sb} - \theta) - 2\cos(\psi)\cos(\phi_{sb} - \theta),$$

$$\alpha_{yb}(\theta) = -\frac{2(mvT_s - \Delta_x)}{L'} \cos(\theta_{sb})\cos(\phi_{sb} - \theta) + 2\cos(\psi)\cos(\theta_{sb})\sin(\phi_{sb} - \theta) + 2\sin(\psi)\sin(\theta_{sb}),$$

θ is a pose angle, ψ is the slant angle, and θ_{sb}, ϕ_{sb} are polar and azimuthal angles. We will consider specular reflector only for targets with unknown pose, because the SAR return signal from a dihedral reflector for arbitrary pose angle has not been developed.

The signal, $\mathbf{r}(m,\tau)$ is continuous in τ(range), circulo-complex and polarimetric. To apply the method of analyzing the performance for FLIR imagery to the SAR case, the raw signal is sampled in the range domain with period equal to the range resolution:

$$\mathbf{x}_{ij}(\theta) = \mathbf{r}(i, j\tau_{res}; \theta). \tag{5.9}$$

We now have a signal model similar to the one for the FLIR case, assuming we have

only additive Gaussian noise as a source of radar-return corruption:

$$\mathbf{x}_{ij}(\theta) = \mathbf{x}^*_{ij}(\theta) + \mathbf{n}_{ij}. \tag{5.10}$$

Since $\mathbf{x}_{ij}$ is a polarimetric complex vector, we define the squared distance measure as follows:

$$E_k(\theta, \theta_1) = \|\mathbf{x}_k(\theta) - \mathbf{x}_1(\theta_1)\|^2 = \sum_{i,j} (\mathbf{x}_{k,ij}(\theta) - \mathbf{x}_{1,ij}(\theta_1))^\dagger (\mathbf{x}_{k,ij}(\theta) - \mathbf{x}_{1,ij}(\theta_1)). \tag{5.11}$$

Table 5.2 and Figure 5-1 specify the target constellation for an example we will discuss. Note that all target components are specular. When target 1 is at pose $\theta_1 = 0$, it has a substantial target return that is due primarily to its component 2, in that this component is perpendicular to the radar line-of-sight. Because target 2 consists of four speculars, each giving very narrow-angle returns which peak at their specular (Snell's law) directions, $E_2(\theta, 0)$ is flat except where one of target 2's components is close to perpendicular to the radar line-of-sight. As can be seen in Figure 5-2, these features appear at $\theta = 8°$, $105°$, $166°$, $285°$, consistent with the azimuthal angles of target 2's components. The minimum $E_2(\theta, 0)$ is at $\theta = 285°$, where target 2's component 3 is normal to the radar line-of-sight.

Figure 5-3 shows the conditional probability of error, $\mathrm{P}(e|H_1, theta_1)$, with respect to SNR. The preceding approximation for the conditional error-probability can be extended to obtain the unconditional error-probability $\Pr(e|H_1)$. If we assume a uniform pose prior, we can obtain:

$$\Pr(e|H_1) = \int_{\theta_{min}}^{\theta_{max}} \Pr(e|H_1, \theta_1)\pi(\theta_1)d\theta_1 \tag{5.12}$$

$$\approx \frac{4\sigma^2|\Theta|^{-1}}{D(\theta^*)^{3/2}\sqrt{D(\ddot{\theta}^*)}} \tag{5.13}$$

	Target 1	Target 2
Component 1 (Δ_x, Δ_y)	(3.0 m, 0 m)	(2.8 m, -0.3 m)
Component 1 ρ_t	0.5	1.0
Component 1 ϕ_{sb}	0.0°	15.0°
Component 1 θ_{sb}	45.0°	40.0°
Component 2 (Δ_x, Δ_y)	(0.0 m, 3.0 m)	(0.3 m, 3.5 m)
Component 2 ρ_t	0.5	0.6
Component 2 ϕ_{sb}	−90.0°	−82.0°
Component 2 θ_{sb}	45.0°	48.0°
Component 3 (Δ_x, Δ_y)	(-3.0 m, 0.0 m)	(-2.5 m, 0.6 m)
Component 3 ρ_t	0.5	0.35
Component 3 ϕ_{sb}	180.0°	195.0°
Component 3 θ_{sb}	45.0°	45.0°
Component 4 (Δ_x, Δ_y)	(0.0 m, -3.0 m)	(-0.3 m, -3.7 m)
Component 4 ρ_t	0.5	0.7
Component 4 ϕ_{sb}	90.0°	76.0°
Component 4 θ_{sb}	45.0°	47.0°

Table 5.1: Specification of target constellation for the example in section 5.2

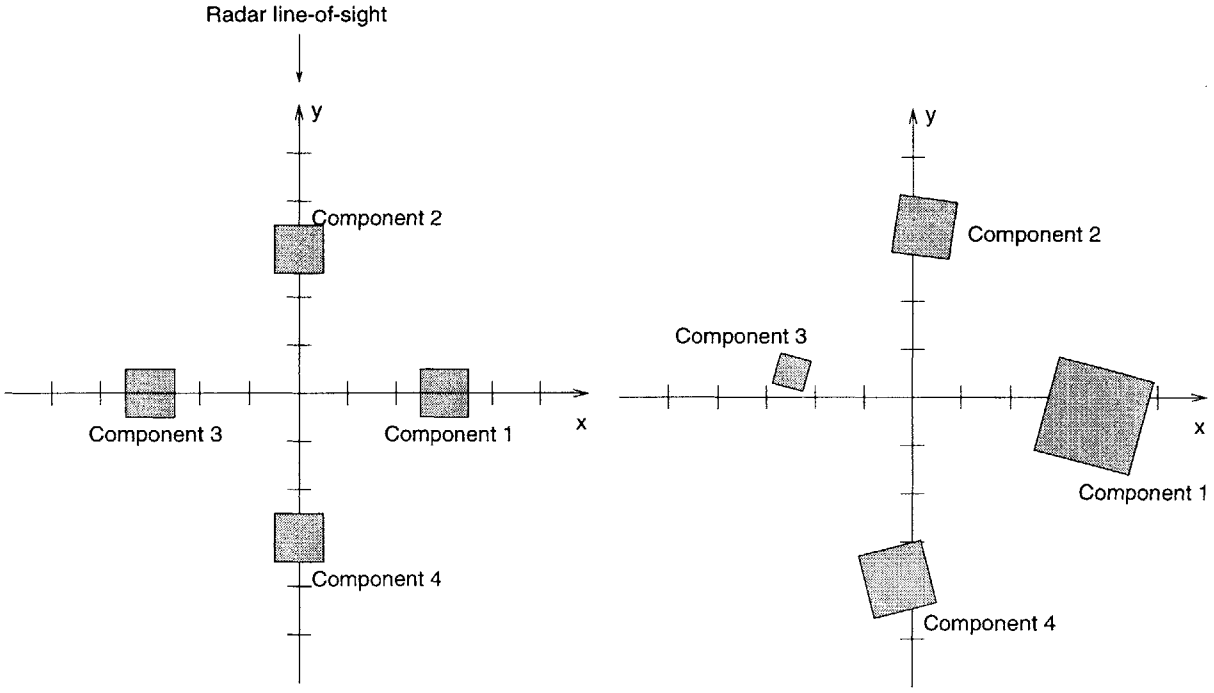

Figure 5-1: Target constellations: target 1 (left) and target 2 (right)

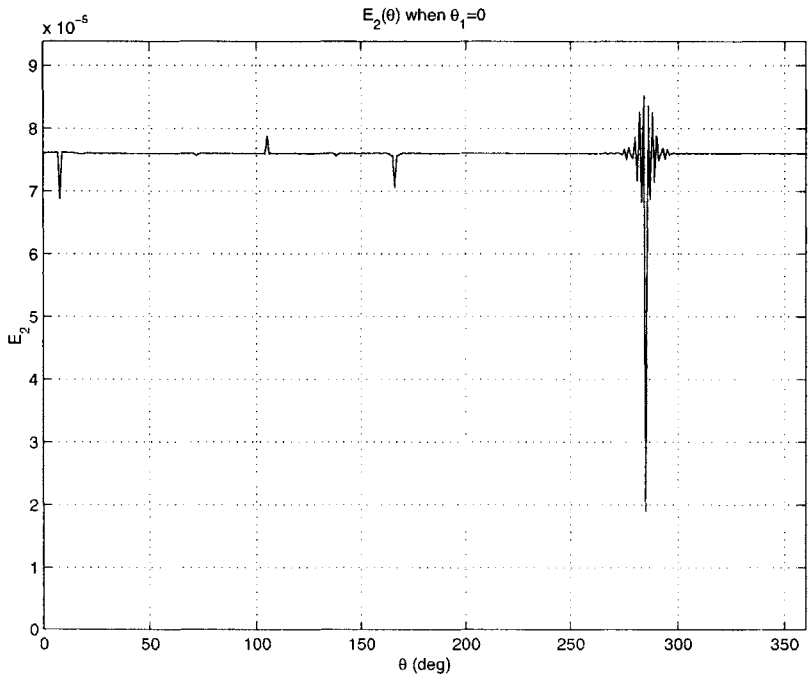

Figure 5-2: Plot of $E_2(\theta)$ vs. θ when the true pose of target 1, $\theta_1 = 0$

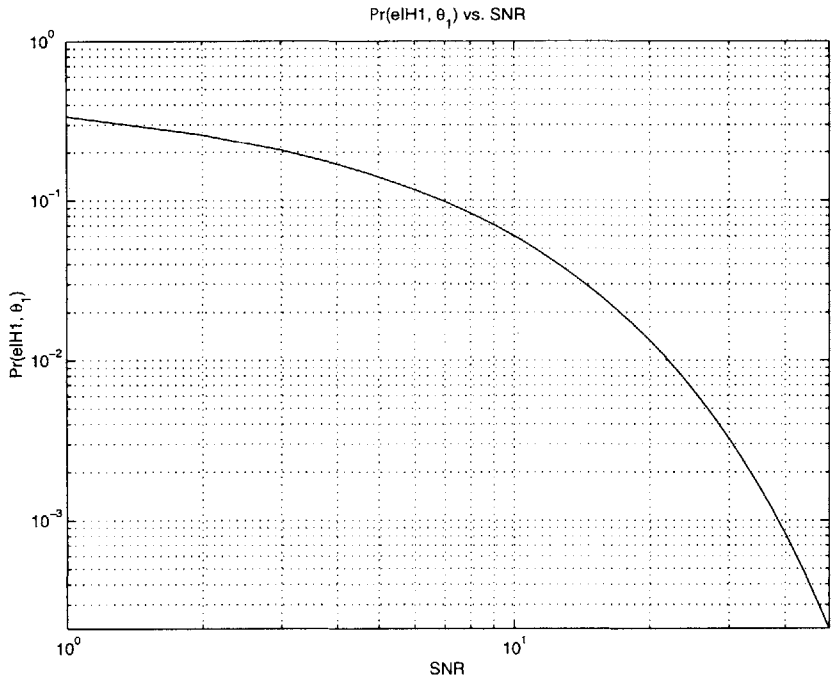

Figure 5-3: Plot of $\mathrm{P}(e|H_1, \theta_1)$ vs. SNR when the true pose of target 1, $\theta_1 = 0$

Chapter 6

Conclusion

6.1 Summary

This thesis has developed methods for assessing the target-classification performance of a SAR-based ATR for specific target-constellation conditions. The contribution of this study is not one of new efficient or powerful processing schemes for real radar data or complicated target signatures generated from CAD models. Instead, it seeks to theoretically quantify the target-recognition performance improvement of adaptive-resolution, polarimetric, or whitening-filter processing. In particular, we have focused on performance analysis for three types of target conditions: (1) targets consisting of a known constellation of reflector components at known absolute locations; (2) targets consisting of a constellation of known reflector components which are located at random positions within some limited, prescribed uncertainty regions; and (3) targets consisting of a constellation of known reflector components with known centroid location but unknown rotation about that centroid. For settings 1 and 2, we obtained a lower bound on PCC from the performance of a recognition processor that makes component-wise reflector decisions, and we obtained an upper bound on PCC by assuming that the returns from target components have known relative phases. Computer simulations showed that the lower bound is very close to the exact result. For setting 3, we used the Laplace approximation to obtain an approximation to PCC that is valid at high signal-to-noise ratios. On the whole, the optimum whitening-

filter processor has approximately 3 to 6 dB gain in terms of SNCR compared to the conventional full-resolution processor, for the examples we considered. A major contribution of this thesis work is that the proposed approximation / bounds on PCC do not incur restrictive target constellation conditions.

6.2 Suggestions for Future Work

Thus far, we have assumed that the target return signals from different target components are orthogonal (2.2). By this assumption we restricted the target setting to be one in which each target reflector is far apart from the others. Removing this restriction is a significant open problem.

The major object of this thesis work was to analyze target classification performance on the foundation of rigorous, physics-based signal models developed from electromagnetic scattering theory and to highlight the performance improvement of a multi/adaptive-resolution processor with respect to a conventional full-resolution processor. Thus, geometrically-simple reflector models (specular and dihedral) suffice for our task. Adding more realistic reflector models in the repertoire can be worthwhile. For example, including trihedrals and dielectric volumes should be possible, as well as performing PCC-bound calculations for target geometries containing many more components than the three or four that we used in our examples.

Our coverage on the performance assessment for targets with unknown rotation angle was limited in that we assumed that each reflector is a specular, all component phases are known. We ignored the clutter as a possible source of radar-return contamination. Also, only conditional probability of error was discussed, and even that discussion was limited to binary recognition. All of these restrictions should be removed in future work.

Bibliography

[1] W. G. Carrara, R.S. Goodman, and R. M. Majewski. *Spotlight Synthetic Aperture Radar: Signal Processing Algorithms.* Artech House, Boston, 1995.

[2] L. M. Novak, S. D. Halversen, G. J. Owirka, and M. Hictt. Effects of polarization and resolution on the performance of a SAR automatic target recognition system. *The Lincoln Laboratory Journal*, 8:49–68, 1995.

[3] H. R. Park, J. Li, and H. Wang. Polarization-space-time domain generalized likelihood ratio detection of radar targets. *Signal Processing*, 41:153–164, 1995.

[4] M. W. Tu, I. J. Gupta, and E. K. Walton. Application of maximum likelihood estimation to radar imaging. *IEEE Transactions on Antennas and Propagation*, 45(1):20–27, 1997.

[5] T. Soni, J. R. Zeidler, and W. H. Ku. Performance evaluation of 2-D adaptive prediction filters for detection of small objects in image data. *IEEE Transactions on Image Processing*, 2(3):327–340, 1993.

[6] W. Irving, R. B. Washburn, and W. E. L. Grimson. Bounding performance of peak-based target detectors. *Proceedings of SPIE*, 3070:245–257, 1997.

[7] J. S. Lee and K. Hoppel. Principal components transformation of multifrequency polarimetric SAR imagery. *IEEE Transactions on Geoscience and Remote Sensing*, 30(7):686–696, 1992.

[8] L. M. Novak, M. C. Burt, R. D. Chaney, and G. J. Owirka. Optimal processing of polarimetric synthetic-aperture radar imagery. *The Lincoln Laboratory Journal*, 3:273–290, 1990.

[9] N. S. Subotic, B. J. Thelen, J. D. Gorman, and M. F. Reiley. Multiresolution detection of coherent radar targets. *IEEE Transactions on Image Processing*, 6(1):21–35, 1997.

[10] C.-P. Yeang. *Target identification theory for synthetic aperture radar images using physics-based signatures*. PhD thesis, MIT, 1999.

[11] G. Leung and J. H. Shapiro. Toward a fundamental understanding of multiresolution SAR signatures. *Proceedings of the SPIE*, 3070:100–109, 1997.

[12] D. C. Munson, J. D. O'Brien, and W. K. Jenkins. A tomographic formulation of spotlight-mode synthetic aperture radar. *Proceedings of the IEEE*, 71(8):917–925, 1983.

[13] G. E. Séguin. A lower bound on the error probability for signals in white Gaussian noise. *IEEE Transactions on Information Theory*, 44(7):3168–3175, Nov 1998.

[14] S. O. Rice. Distribution of the duration of fades in radio transmission. *Bell System Technology Journal*, 37:581–635, 1958.

[15] V. I. Tikhonov. The Markov nature of the envelope of quasiharmonic oscillations. *Radio Engineering and Electronic Physics*, 6:961–971, 1961.

[16] J. H. Shapiro, R. W. Reinhold, and D. Park. Performance analyses for peak-detecting laser radars. *Proceedings of SPIE*, 663:38–56, 1990.

[17] U. Grenander, A. Srivastava, and M. Miller. Asymptotic performance analysis of Bayesian target recognition. *IEEE Transactions on Information Theory*, 46:1658–1665, 2000.

[18] B. J. Yen. *Target Recognition Performance for FLIR and Laser Radar Systems*. M.Eng. thesis, MIT, 2000.

[19] H. L. Van Trees. *Detection, estimation and modulation theory: Part III.* Wiley, New York, 1971.

[20] D. Park and J. H. Shapiro. Performance analysis of optical synthetic aperture radars. *Proceedings of SPIE*, 999:100–116, 1988.

[21] D. C. Munson and R. L. Visentin. A signal-processing view of strip-mapping synthetic aperture radar. *IEEE Transactions on Acoustics, Speech, and Signal Processing*, 37(12):2131–2147, 1990.

[22] W. W. Irving, L. M. Novak, and A. S. Willsky. A multiresolution approach to discriminating targets from clutter in SAR imagery. *Proceedings of the SPIE*, 2487:272–299, 1995.